RESEARCH ARTICLE

Human ASXL1-Mutant Hematopoiesis Is Driven by a Truncated Protein Associated with Aberrant Deubiquitination of H2AK119

Thomas Köhnke[1,2], Kevin A. Nuno[1,2], Catherine C. Alder[2], Eric J. Gars[1,2], Paul Phan[1,2], Amy C. Fan[1,2], and Ravindra Majeti[1,2]

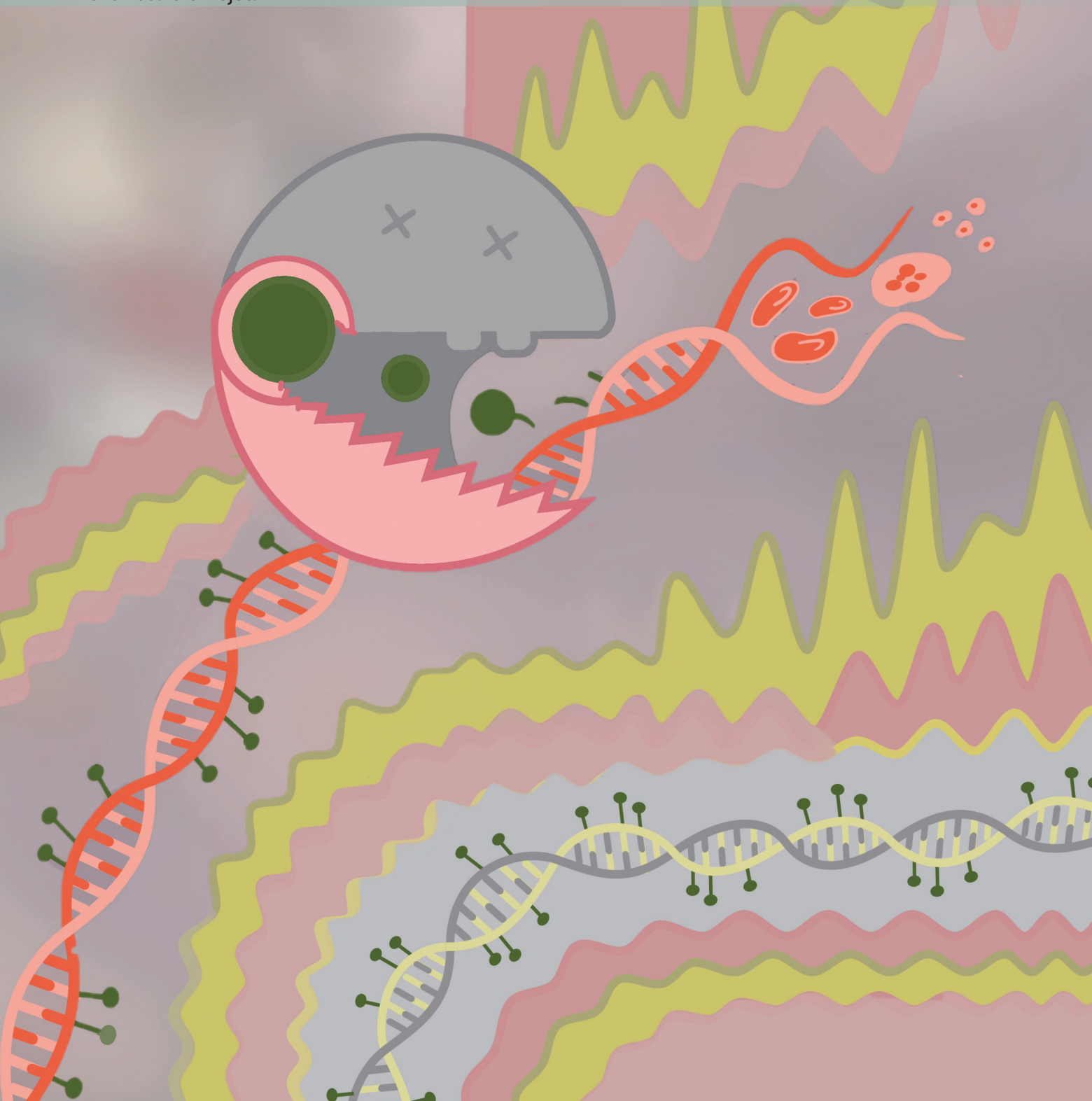

ABSTRACT Mutations in *additional sex combs like 1* (*ASXL1*) confer poor prognosis both in myeloid malignancies and in premalignant clonal hematopoiesis (CH). However, the mechanisms by which these mutations contribute to disease initiation remain unresolved, and mutation-specific targeting has remained elusive. To address this, we developed a human disease model that recapitulates the disease trajectory from ASXL1-mutant CH to lethal myeloid malignancy. We demonstrate that mutations in *ASXL1* lead to the expression of a functional, truncated protein and determine that truncated ASXL1 leads to global redistribution of the repressive chromatin mark H2AK119Ub, increased transposase-accessible chromatin, and activation of both myeloid and stem cell gene-expression programs. Finally, we demonstrate that H2AK119Ub levels are tied to truncated ASXL1 expression levels and leverage this observation to demonstrate that inhibition of the PRC1 complex might be an ASXL1-mutant–specific therapeutic vulnerability in both premalignant CH and myeloid malignancy.

SIGNIFICANCE: Mutant ASXL1 is a common driver of CH and myeloid malignancy. Using primary human HSPCs, we determine that truncated ASXL1 leads to redistribution of H2AK119Ub and may affect therapeutic vulnerability to PRC1 inhibition.

INTRODUCTION

Mutations in *additional sex combs like 1* (*ASXL1*) are recurrently found in myeloid malignancies including chronic myelomonocytic leukemia (1), myelodysplastic syndromes (2), and acute myeloid leukemia (AML; refs. 3, 4), in which they confer very poor prognosis and treatment response. We and others have implicated *ASXL1* mutations as frequent initiating events during leukemogenesis (5, 6). In line with this observation, *ASXL1* mutations are also commonly found in premalignant clonal hematopoiesis (CH; refs. 7–9). *ASXL1* mutations typically occur as frameshift mutations in the central portion of the gene, resulting in the early introduction of a nonsense mutation (10). Although initial observations suggested a loss of function of the ASXL1 protein as relevant to disease (11), several studies have suggested that recurrent *ASXL1* mutations result in a truncated protein with aberrant functions (12–15). Most of these studies have been performed in cell line or mouse model systems with overexpression of truncated ASXL1 with inconsistencies between models; cells with truncated ASXL1 showed clonal expansion in some models (12, 14) but were outcompeted by wild-type cells in other models (13, 15, 16). Thus, the mechanisms by which mutant ASXL1 contributes to CH and leukemogenesis remain unsettled.

The function of ASXL1 in chromatin remodeling has been well described where together with the deubiquitinase BAP1, ASXL1 forms the polycomb repressive–deubiquitinase (PR-DUB) complex. The PR-DUB complex removes ubiquitin from histone 2A (H2A) at lysine 119 (17, 18), which is in turn deposited by the polycomb repressive complex 1 (PRC1). H2AK119Ub is one of the most prevalent histone marks, characteristic of repressed developmental genes, and linked to the repressive histone mark H3K27me3 (19, 20). In mammals, the ASXL family is comprised of ASXL1, ASXL2, and ASXL3. ASXL1 and ASXL2 are widely expressed in most tissues, whereas ASXL3 expression is more restricted and is mostly found in the brain (21). Germline mutations in *ASXL1* and *ASXL3* have been associated with neurodevelopmental disorders (22, 23), and whereas somatic mutations in *ASXL1/2/3* can be found in various nonhematopoietic cancers, most mutations found in ASXL family proteins are found in clonal hematopoietic disorders (21). However, how mutations in *ASXL1* alter the activity of the PR-DUB complex, as well as the distribution of H2AK119Ub in primary human HSPCs, and whether this is correlated with chromatin states and gene-expression programs is unknown.

Disease prevention and therapeutic targeting of mutant *ASXL1* have remained elusive because of a poor understanding of disease mechanisms, lack of representative model systems, and lack of promising therapeutic targets. In this study, we address these issues by exploring the effects of *ASXL1* mutations in human HSPCs. We use CRISPR/Cas9 genome engineering of primary human HSPCs to show that *ASXL1* mutations lead to increased self-renewal, competitive advantage, myeloid skewing, and spontaneous progression to myeloid malignancy. Moreover, we demonstrate that mutations in the central portion of *ASXL1* phenocopy human disease *in vitro* and *in vivo* through the production of a truncated protein leading to increased activity of the PR-DUB complex and a global reduction and redistribution of H2AK119Ub. Finally, we demonstrate that alteration of H2AK119Ub levels affects ASXL1-mutant phenotypes with drastic reduction through pharmacologic and genetic inhibition of PRC1 leading to decreased cell viability.

[1]Department of Medicine, Division of Hematology, Cancer Institute, and Institute for Stem Cell Biology and Regenerative Medicine, Stanford University, Stanford, California. [2]Stanford School of Medicine, Stanford, California.

Corresponding Author: Ravindra Majeti, Department of Medicine, Division of Hematology, Cancer Institute, and Institute for Stem Cell Biology and Regenerative Medicine, Stanford University School of Medicine, 265 Campus Drive, G3021B, Stanford, CA 94305. E-mail: rmajeti@stanford.edu

Blood Cancer Discov 2024;5:202–23

doi: 10.1158/2643-3230.BCD-23-0235

RESULTS

Mutations across the ASXL1 Coding Sequence Are Preserved across Disease States

Mutations in *ASXL1* are frequently found in both CH and myeloid malignancies (3, 4, 7), suggesting that these mutations can act as the initiating lesion in AML. Indeed, we previously identified residual preleukemic HSCs in patients with AML that shared some but not all mutations found in the leukemic clone (5). These preleukemic clones were enriched for mutations in epigenetic regulators, including mutations found in CH, particularly *DNMT3A*, *TET2*, and *ASXL1*.

To investigate if the functional effects of *ASXL1* mutations are likely to be similar across myeloid malignancies, we first sought to determine if the *ASXL1* mutational spectrum was preserved across the different disease entities. We aggregated publicly available data describing mutations in *ASXL1* from individuals with myelodysplastic syndrome/myeloproliferative neoplasm (MDS/MPN) and AML and only included studies that sequenced the entire *ASXL1* coding region. Using these criteria, we identified 1,442 cases (1,163 for MDS/MPN and 279 for AML; Supplementary Table S1) and summarized all frameshift/nonsense mutations based on their position in the *ASXL1* coding sequence. In addition, we expanded our cohort of genotyped AML samples from our tissue bank by integrating both our previously published (n = 69) targeted genotyping data with targeted genotyping on additional samples (n = 118) for a total cohort of 187 primary AML samples (Supplementary Fig. S1; Supplementary Table S2).

This analysis demonstrated that more than 95% of mutations occur in the center of the coding sequence between amino acids 410 and 1140 (Fig. 1A). In addition, the distribution of mutations was similar across disease entities with the majority occurring in the hotspot region around amino acid 646. Finally, the mutations found in our Stanford cohort (n = 22) closely mirrored these published cohorts, illustrating that the samples in our biobank are representative of the broad AML population (Fig. 1A). Together, *ASXL1* frameshift or nonsense mutations are predominantly found in the central coding region and, interestingly, spare the functional DEUBAD domain in both MDS/MPN and AML.

CRISPR/Cas9 Screening across the ASXL1 Coding Sequence in Human HSPCs

The enrichment of *ASXL1* mutations in the center of the coding sequence in clinical specimens suggests that the localization might have functional implications. However, to date, functional experiments prospectively addressing this question in human hematopoiesis are lacking. Thus, we utilized CRISPR/Cas9 in primary human cord-blood–derived CD34$^+$ HSPCs to introduce mutations across the *ASXL1* coding sequence. After purifying CD34$^+$ HSPCs from cord-blood donors, we split CD34$^+$ cells into 10 equal fractions and electroporated each fraction with purified recombinant Cas9 protein precomplexed with 1 of 10 single-guide RNAs (sgRNA) equally spaced across the *ASXL1* coding sequence (Fig. 1B). After electroporation, the cells were mixed together again for *in vitro* and *in vivo* functional assays. All 10 sgRNAs resulted in detectable editing (measured as the fractional abundance of frameshift insertions/deletions at the respective loci 48h after engineering by amplicon sequencing; Supplementary Fig. S2A). Next, we subjected the cells to a serial replating assay *in vitro* and determined the fractional abundance of frameshift alleles after each replating (Fig. 1C). Frameshift alleles in early or late regions of the coding sequence were lost over time, whereas the fractional abundance of frameshift alleles in the center of the coding sequence increased with each replating (Fig. 1D). In parallel, we transplanted the pooled cells into immunodeficient NSGS mice (n = 5) and determined the fractional abundance of frameshift alleles at each locus in the lymphoid (CD19$^+$) and myeloid (CD33$^+$) progeny engrafted at 12 weeks (Fig. 1E). In these experiments, frameshift alleles in the center of the coding sequence were overrepresented in the human myeloid versus lymphoid engrafted cells, demonstrating a myeloid skewing of cells with frameshift alleles in the center of *ASXL1* (Fig. 1F).

Because recurrent mutations in ASXL1 in human disease are almost exclusively heterozygous, we next characterized the zygosity of our engineered CD34$^+$ HSPCs at the ASXL1 locus. For this set of experiments, we focused on the locus showing the greatest expansion in our pooled experiments and performed CRISPR/Cas9-engineering on CD34$^+$ HSPCs using sgRNA 5. At this locus, we detected an average fraction of frameshift alleles of 30% in 4 independent cord-blood specimens (Supplementary Fig. S2B). Next, to determine the zygosity of individual HSPC clones, we single-cell–sorted CD34$^+$ HSPCs immediately after CRISPR/Cas9-engineering and genotyped these single-cell–derived clones 7 days later (Supplementary Fig. S2C). In clones with detectable frameshift insertions/deletions, 86% were heterozygous and 14% were homozygous (Supplementary Fig. S2D and S2E). Finally, phenotyping of these single-cell–derived clones showed increased retention of CD34 *in vitro* for heterozygous mutant cells compared with wild-type (Supplementary Fig. S2F).

In summary, this set of experiments demonstrates that mutations in the central regions of *ASXL1* impart increased serial replating capacity *in vitro* and myeloid skewing *in vivo*. Importantly, these phenotypes were not observed for mutations in the early coding region, suggesting that mutations in *ASXL1* might not act as loss of function but rather could be mediated by a truncated ASXL1 protein. Lastly, we see that the HSPCs subjected to CRISPR/Cas9 engineering at the center of the *ASXL1* coding sequence primarily have heterozygous frameshift alleles, mirroring the genotype found in human disease.

Engineered Human HSPCs Mimic Human ASXL1-Mutated CH *In Vitro*

In order to further compare loss of function to truncation of *ASXL1* and characterize their functional effects directly in human HSPCs, we utilized our recently established approach combining CRISPR/Cas9-genome targeting with recombinant AAV6 (rAAV6)–mediated delivery of a homology-directed repair template allowing for insertion of a traceable fluorescent marker in successfully engineered HSPCs (24). Similar to the engineering strategy used above, recombinant Cas9 protein and guide RNA targeting the genomic locus of interest were precomplexed and electroporated into normal human cord-blood–derived CD34$^+$ HSPCs. These cells were then infected

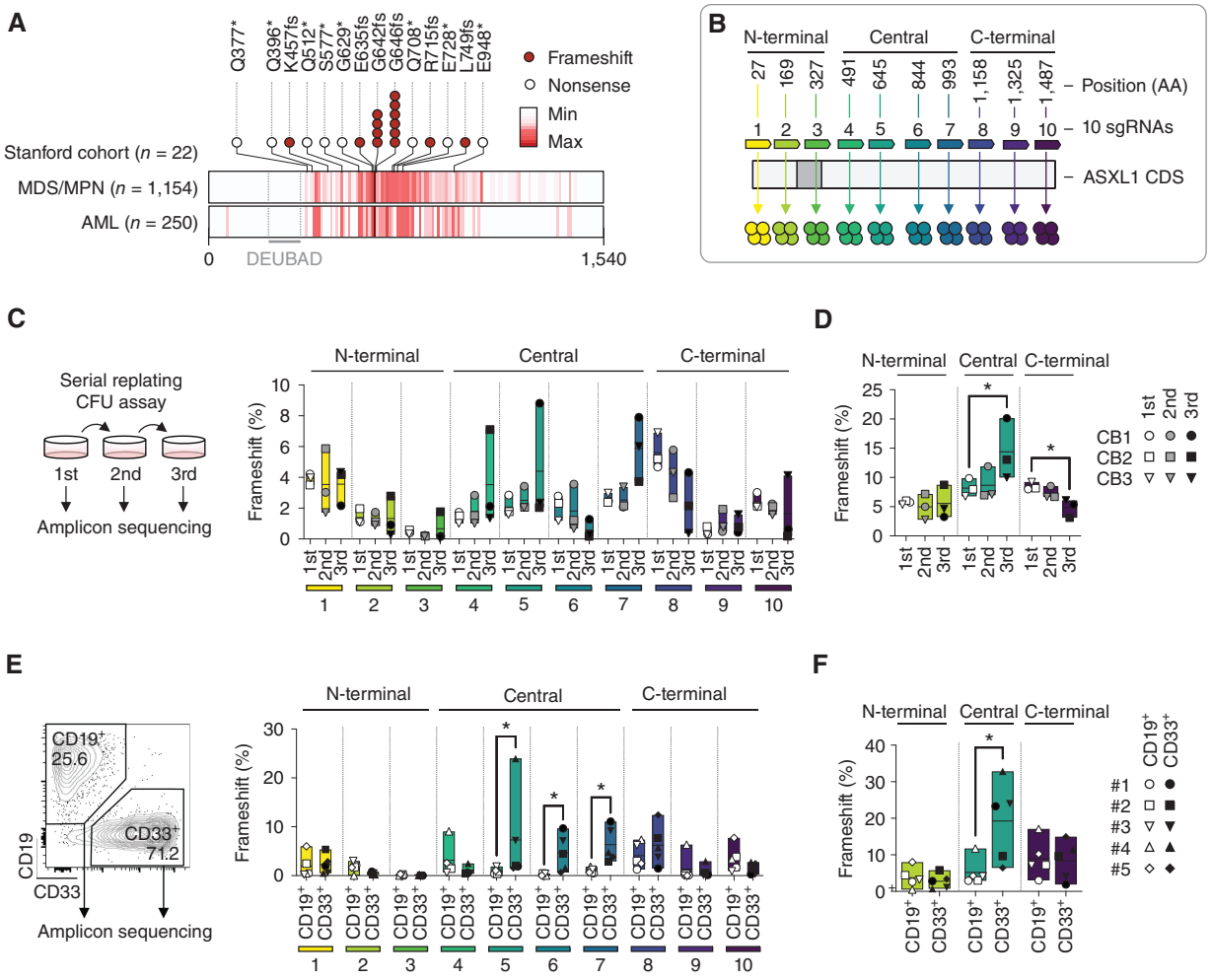

Figure 1. Mutations in ASXL1 frequently occur at the center of the coding sequence. **A,** Lollipop plot (top) and heat map (bottom) of the ASXL1 coding sequence across the disease spectrum of myeloid malignancies. Published data from 1,404 cases with ASXL1 mutations as well as 22 cases from our Stanford AML cohort are aggregated according to their relative position along the ASXL1 coding sequence. DEUBAD denotes the DEUBiquitinase Adaptor domain of ASXL1. **B,** Schematic of CRISPR/Cas9-based engineering of human CD34+ HSPCs with 10 single-guide RNAs (sgRNAs) tiled along the *ASXL1* coding sequence, annotated for sgRNAs targeting the N-terminal, central, or C-terminal region of ASXL1. **C,** Frequency of frameshift insertions/deletions detected in engineered cord-blood–derived cells following colony formation replating assays ($n = 3$ independent cord-blood donors) for each of the 10 sgRNA target sites. **D,** Sum of all frameshift alleles found in the N-terminal (sgRNAs 1–3), central (sgRNAs 4–7), or C-terminal (sgRNAs 8–10) regions of ASXL1 after first, second, and third replating; statistical significance was determined by the FDR-corrected *t* test. **E,** Frequency of frameshift insertions/deletions detected in sorted human (hCD45+) lymphoid (CD19+) or myeloid (CD33+) cells at 12 weeks after engraftment in NSG mice ($n = 5$ independent mice); statistical significance determined by FDR-corrected Wilcoxon test. **F,** Sum of all frameshift alleles found in the N-terminal, central, or C-terminal regions of ASXL1; statistical significance was determined by the FDR-corrected *t* test. *, $P < 0.05$.

with an rAAV6 viral vector carrying flanking arms of homology and a traceable marker, and cells were subsequently purified for *in vitro* and *in vivo* experiments by flow cytometry (Fig. 2A, top). For this set of experiments, two targeting strategies were designed: the first targeting exon 12 of *ASXL1* and creating a truncated protein (ASXL1 truncation); the second targeting exon 2 knocks out the ASXL1 protein (ASXL1 KO). As a control, a noncoding region on chromosome 19 (*AAVS1*, a "safe harbor" locus) was targeted. Each targeting vector contains a different fluorescent marker to allow clonal tracking for competition experiments (Fig. 2A, bottom). Using this approach, we obtained average genome engineering efficiencies ranging from 42% to 65% in primary human CD34+ HSPCs (Fig. 2B). Detection of the truncated ASXL1 protein with commercially available reagents is challenging, and investigators have resorted to developing custom antibodies (25, 26). Indeed, when we performed standard Western blotting on leukemia cell lines using two commercially available antibodies targeting ASXL1 (one C-terminal and one N-terminal), Western blots showed multiple bands and only inconsistently detected full-length ASXL1 (Supplementary Fig. S3A). Thus, to determine if the truncated protein is in fact expressed in our engineered HSPCs, we included a C-terminal hemagglutinin (HA) tag in our ASXL1 truncation vector inserted in-frame into the ASXL1 coding sequence (Supplementary Fig. S3B). Using this strategy, we were able to detect the expression of the truncated ASXL1 protein in our engineered HSPCs by western blot for the HA tag (Fig. 2C; Supplementary Fig. S3C).

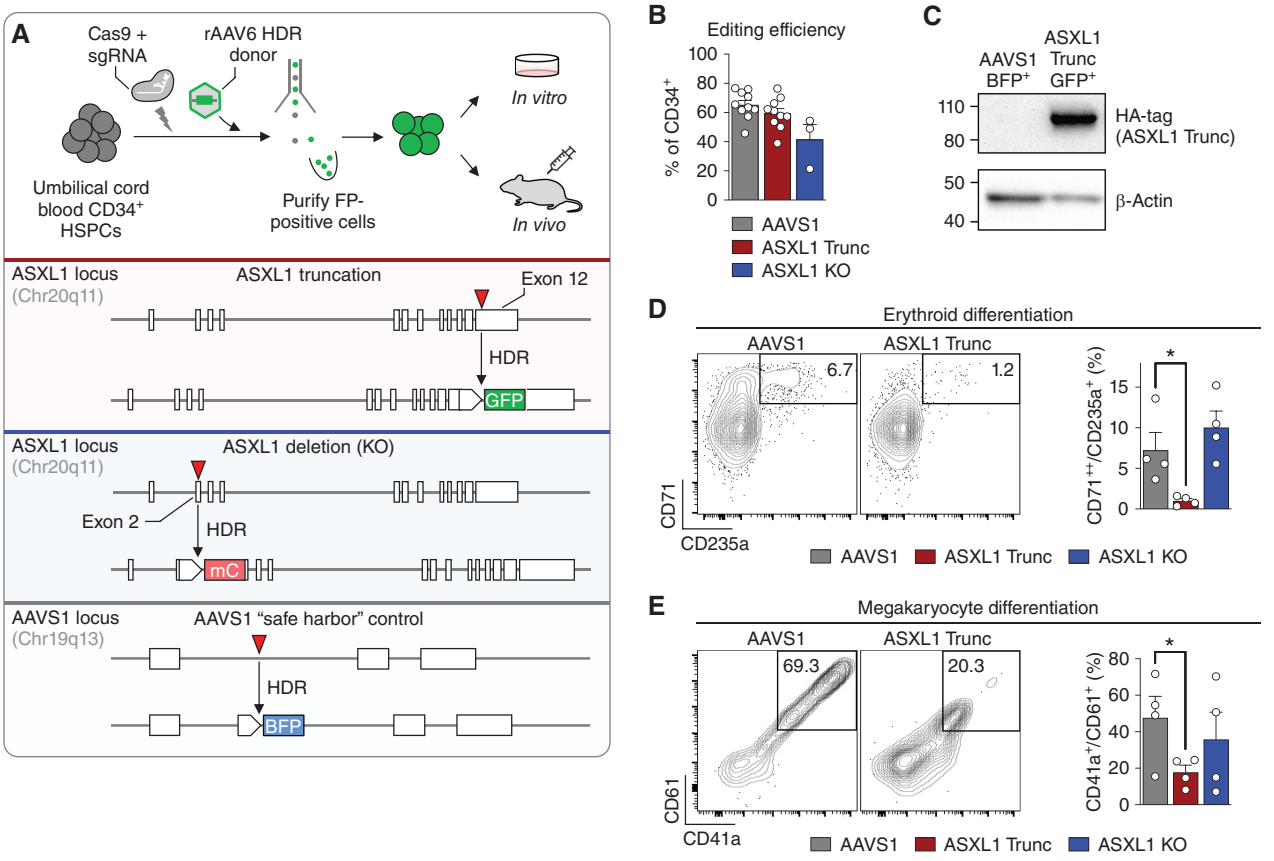

Figure 2. Induction of truncating *ASXL1* mutations in human CD34+ HSPCs mimics human *ASXL1*-mutated clonal hematopoiesis. **A,** Schematic of engineering strategy for editing primary human CD34+ HSPCs. **B,** Editing efficiency in human, cord-blood–derived CD34+ HSPCs determined by flow cytometry ($n = 10$ donors for AAVS1 and ASXL1 Trunc and $n = 3$ donors for ASXL1 KO). **C,** Western blot detecting HA-tagged truncated ASXL1 (top) as well as β-actin loading control (bottom) in AAVS1 control (lane 1), ASXL1 Trunc (lane 2) HSPCs. **D,** Percentage of $CD71^{++}/CD235a^{+}$ positive erythroblasts in liquid culture at 10 days of erythroid differentiation media, statistical significance determined by Student *t* test. **E,** Percentage of $CD41a^{+}/CD61^{+}$ megakaryocytes at 10 days in liquid megakaryocyte differentiation media; statistical significance was determined by the Student *t* test. (*continued on following page*)

Next, we subjected these cells to erythroid (Fig. 2D) and megakaryocytic (Fig. 2E) differentiation assays *in vitro*. Here, HSPCs with truncated ASXL1 showed a marked reduction in their capacity to differentiate into $CD71^{++}/CD235a^{+}$ erythroblasts, as well as $CD41a^{+}/CD61^{+}$ megakaryocytes compared with both AAVS1 control and ASXL1 KO cells. When subjected to a myeloid differentiation assay, there was no significant difference in myeloid progeny (Supplementary Fig. S4A). Next, we performed colony-forming assays in cytokine-containing semisolid methylcellulose media. Similar to our liquid culture experiments, human HSPCs with truncated ASXL1 were less likely to form erythroid colonies (Fig. 2F), whereas ASXL1 KO cells showed no such defect. Although cells with truncated ASXL1 did not form an increased number of myeloid colonies (Fig. 2F, right), we observed an increased size of colonies compared with AAVS1 control (Supplementary Fig. S4B and S4C). Next, we performed serial replating assays and found that HSPCs with truncated ASXL1 showed a marked increase in replating capacity compared with AAVS1 control cells (Fig. 2G). Finally, we determined the ability of HSPCs with truncated ASXL1 to proliferate *in vitro*. In liquid culture, HSPCs with truncated ASXL1 outgrew AAVS1 control cells (Supplementary Fig. S4D) while retaining a higher fraction (Fig. 2H), as well as fold expansion (Supplementary Fig. S4E) of $CD34^{+}$ cells after 7 days of liquid culture. Finally, we confirmed whether the length of the truncated ASXL1 protein correlated with the functional phenotypes in our $CD34^{+}$ HSPC system. We performed engineering of human $CD34^{+}$ HSPCs with either AAVS1 control, ASXL1 KO, ASXL1 Trunc, or a very late truncation in ASXL1, leaving all but the C-terminal zinc finger domain of the protein intact. Notably, the late truncation in ASXL1 did not result in decreased erythroid colony formation, as seen with the typical truncation (Supplementary Fig. S4F).

Taken together, these assays highlight that HSPCs with truncated ASXL1 exhibit a defect in erythroid and megakaryocytic differentiation, an increase in replating potential, and a proliferative advantage compared with control cells. Importantly, ASXL1 KO cells did not show these phenotypes.

Engineered Human HSPCs Mimic Human ASXL1-Mutated CH *In Vivo*

Next, we performed competitive transplant experiments *in vivo*, by mixing $CD34^{+}$ HSPCs with truncated ASXL1 with

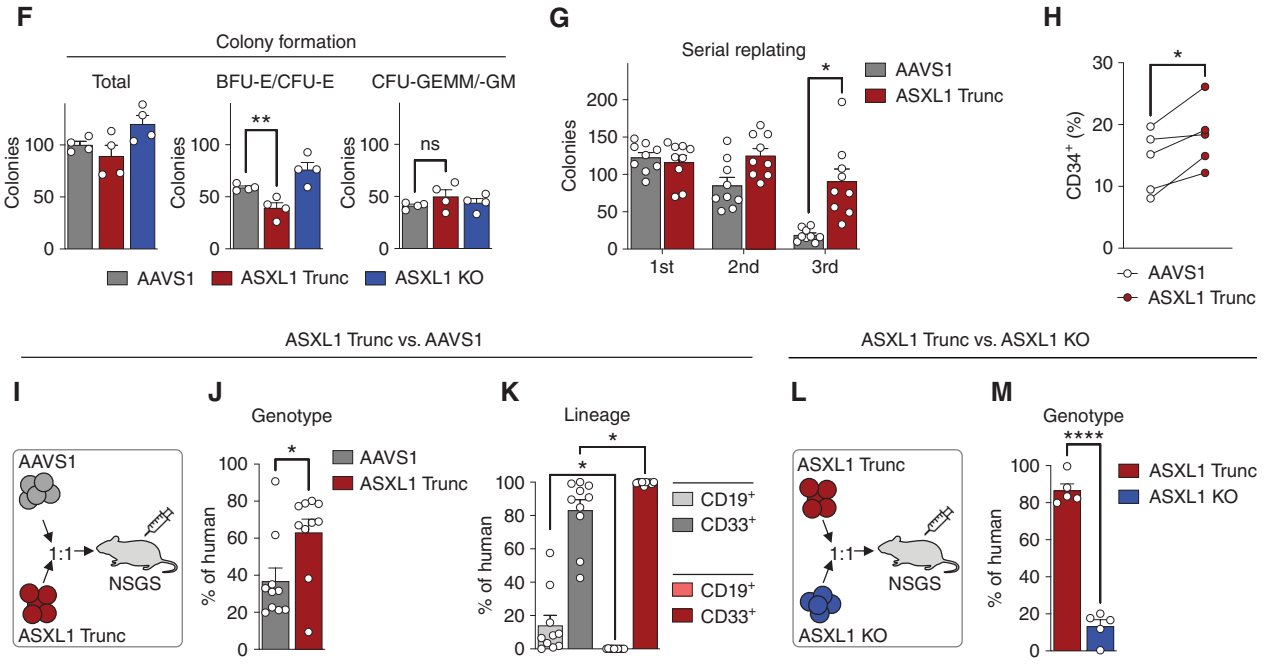

Figure 2. ***(Continued)*** **F,** Total number of colonies at 14 days in MethoCult semisolid methylcellulose assay (left), scored by morphology as BFU-E/CFU-E (middle) or CFU-GEMM/CFU-GM (right; $n = 4$); statistical significance was determined by the Student *t* test. **G,** Colony number during serial replating assays for first, second, and third plating ($n = 9$); statistical significance was determined by the Student *t* test. **H,** Relative percentage of CD34$^+$ cells at 7 days in liquid culture ($n = 5$); statistical significance was determined by the Student *t* test. **I,** Schematic for *in vivo* competitive transplant assays using AAVS1 control (marked by BFP) vs. ASXL1 Trunc (marked by GFP) CD34$^+$ HSPCs into NSGS mice. **J,** Relative contribution in percent of cells marked by BFP (AAVS1 control) or GFP (ASXL1 Trunc) within the human (CD45$^+$) graft in mouse bone marrow at 8 weeks after engraftment ($n = 10$ mice); statistical significance was determined by the Student *t* test. **K,** Lineage (CD19$^+$ B-lymphoid vs. CD33$^+$ myeloid) of either AAVS1 control (gray) or ASXL1 Trunc (red) cells in mouse bone marrow at 8 weeks after engraftment ($n = 10$ mice); statistical significance was determined by the Student *t* test. **L,** Schematic of *in vivo* competitive transplant assays using ASXL1 KO vs. ASXL1 Trunc CD34$^+$ HSPCs. **M,** Relative contribution of ASXL1 KO (marked by mCherry) vs. ASXL1 Trunc (marked by GFP) within the human (CD45$^+$) graft in mouse bone marrow at 8 weeks after engraftment ($n = 5$ mice); statistical significance was determined by the Student *t* test. *, $P < 0.05$; **, $P < 0.01$; ****, $P < 0.0001$; n.s., not significant.

AAVS1 control cells at a 1:1 ratio and transplanting into irradiated NSGS mice (Fig. 2I). At 8 weeks, we determined human chimerism as well as lineage distribution of the human graft. In these assays, mice showed variable but consistent engraftment (Supplementary Fig. S4G). Within the human CD45$^+$ fraction, cells with truncated ASXL1 were significantly more abundant than AAVS1 control cells (Fig. 2J). In addition, cells with truncated ASXL1 did not form any lymphoid progeny in these myeloid-cytokine–expressing NSGS mice, unlike AAVS1 control cells, which produced CD19$^+$ lymphoid progeny (Fig. 2K). Finally, we performed similar competitive transplant studies using CD34$^+$ HSPCs with truncated ASXL1 versus cells with ASXL1 KO (Fig. 2L) and detected a marked competitive disadvantage of cells with ASXL1 KO (Fig. 2M). Taken together, these assays demonstrate that truncating ASXL1 mutations closely phenocopy ASXL1-mutant CH *in vivo*, particularly in their ability to drive clonal outgrowth compared with control HSPCs. Moreover, these studies clearly establish that truncated ASXL1 confers a distinct phenotype from ASXL1 loss of function.

Engineered Human HSPCs Progress into a Lethal, Myeloid Malignancy in a Subset of Mice

In our cohort of mice engrafted with cells engineered to carry truncated ASXL1, we noticed that two mice developed severe lethargy at 105 and 209 days after transplant, respectively (Fig. 3A). These two mice displayed enlarged spleens (Fig. 3B) as well as severe anemia and thrombocytopenia compared with their similarly engrafted littermates (Fig. 3C). Upon sacrifice, we detected high human chimerism in the bone marrow, spleen, and peripheral blood as well as infiltration of nonhematopoietic organs such as lung and liver by human CD45$^+$ cells (Fig. 3D; Supplementary Fig. S5A and S5B). By morphology, these cells showed an immature myeloid phenotype, reminiscent of promyelocytes. This was also reflected by extensive immunophenotyping, in which these cells showed an immature myeloid phenotype, dominated by expression of myeloid markers (CD33, CD11b, CD123, and CD13) but lacking terminal monocytic markers such as CD14 or CD16 (Fig. 3E; Supplementary Fig. S5C). By histology, mouse bone marrow was heavily infiltrated by monomorphic hCD45$^+$ cells (Fig. 3F; Supplementary Fig. S5B). We confirmed on-target insertion of our AAV6 donor template and lack of relevant off-target edits in these cells by next-generation sequencing (NGS), which also showed no evidence of additional genetic alterations in genes recurrently mutated in myeloid malignancies or gross chromosomal copy-number anomalies (Supplementary Fig. S5D). Furthermore, we confirmed the retention of truncated protein expression in myeloid cancer from mouse 871#3 (Supplementary Fig. S3C).

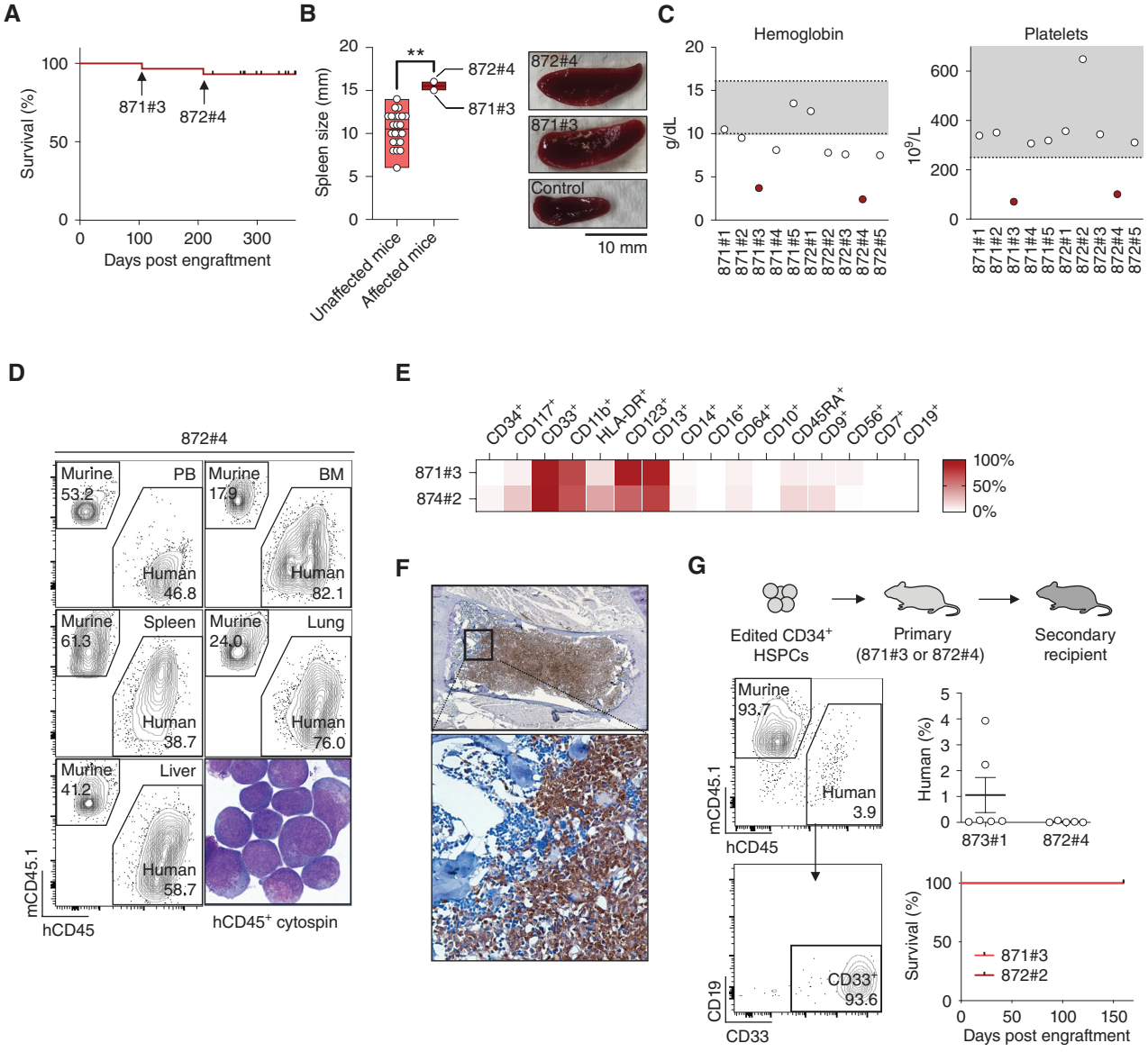

Figure 3. Truncating ASXL1 mutations in human CD34+ HSPCs induce progression to myeloid malignancies in a small subset of cases. **A,** Survival curves of mice engrafted with engineered HSPCs with truncated ASXL1, with mice 871#3 and 872#4 requiring euthanasia at 105 and 209 days after engraftment because of severe lethargia (total no. of mice receiving ASXL1 Trunc cells $n = 29$). **B,** Spleen size of unaffected and affected mice engrafted with ASXL1 Trunc cells at the time of euthanasia; statistical significance was determined by the Student t test. **C,** Hemoglobin (left) and platelets (right) in peripheral blood of sick mice (highlighted in red) and their corresponding littermates. **D,** Flow-cytometric evaluation of peripheral blood (PB), bone marrow (BM), spleen, lung, and liver and cytospin of sorted hCD45+ BM cells stained with May–Grünwald–Giemsa of mouse 872#4. All populations pregated on live Ter119− hematopoietic cells. **E,** Phenotyping by flow cytometry of human (hCD45+) cells recovered from mice 871#3 and 872#4 presented as a percentage of marker-positive cells (underlying flow cytometry plots can be found in Supplementary Fig. S5C). **F,** Bone marrow IHC staining for human CD45. **G,** Secondary transplantation studies for specimens recovered from mice 873#1 and 872#4 and transplanted into irradiated secondary NSGS recipient mice (100k cells per recipient mouse and $n = 5$ mice per specimen). Representative flow cytometry of recipient bone marrow at 5 months after injection (left). Quantification of chimerism in recipient mice by primary specimen (right middle) and survival (bottom right).
**, $P < 0.01$.

Finally, we performed secondary transplantation studies from these two specimens. Here, we found low but detectable myeloid-restricted engraftment in secondary recipients from one of the specimens (Fig. 3G), which, however, did not display a lethal phenotype in the time frame monitored (5 months).

Of note, the remaining cohort of mice, despite being engrafted with similarly engineered human HSPCs, showed normal life spans with stable human engraftment for >8 months. These observations demonstrate that primary human HSPCs harboring truncating ASXL1 mutations are capable of spontaneous progression into a lethal myeloid malignancy but that most engrafted mice do not develop disease, closely mirroring the clinical experience with ASXL1-mutant CH.

Truncation of ASXL1 Induces Myeloid- and Stemness-Related Transcriptional Programs

Next, we aimed to determine the gene-expression profiles of HSPCs with truncating *ASXL1* mutations. We performed RNA-seq on HSPCs 7 days after gene editing and determined differentially expressed genes. We noted that genes involved in erythroid and megakaryocyte pathways (*HBE1, HEMGN*, and *PDGFB*) were downregulated in cells with truncated ASXL1, whereas myeloid genes (*EPX, CD24, CD14*, and *MPO*) were upregulated (Fig. 4A). Indeed, when performing CIBERSORTx-based deconvolution (27) of gene-expression programs from defined hematopoietic cell populations, we observed increased abundance of myeloid programs, especially gene-expression signatures derived from myelocytes (Fig. 4B). Overall, we noted some heterogeneity between cord-blood donors, but on average, cells with truncated ASXL1 showed increased abundance (69%) of gene-expression programs derived from myeloid HSPCs and mature myeloid progeny, whereas AAVS1 control cells showed a higher abundance of erythro/megakaryocytic gene-expression programs (56%; Fig. 4C). When performing hierarchical clustering of normalized gene expression from genes significantly differentially expressed in our engineered human HSPCs, we observed decreased expression of hemoglobin and platelet-related genes (*HBE1* and *PDGFB*), with increased expression of myeloid genes (*CD14* and *MPO*) and genes associated with stem cells (*CD34, HOXA5, HOXA7*, and *HOXA9*) in cells engineered with truncated ASXL1 (Fig. 4D). We confirmed that these differences in gene expression correlated with cell phenotypes by culturing engineered cells in media containing a pan-differentiation cytokine cocktail and phenotyping the resulting cultures by high-parameter flow cytometry after 7 days (Fig. 4E and F). When coclustering the AAVS1 control and ASXL1 truncated cells into the same low-dimensional UMAP space, cells with truncated ASXL1 were more abundant in progenitor, monocytic, and neutrophilic clusters, whereas AAVS1 control cells were more abundant in erythroid clusters (Fig. 4G), in line with our RNA-seq results. These experiments demonstrate that truncating ASXL1 mutations leads to the expression of myeloid- and stemness-related gene programs in primary human HSPCs.

Truncation of ASXL1 Leads to a Global Reduction of H2AK119Ub

Together with BAP1, ASXL1 forms the PR-DUB complex, which removes ubiquitin from H2AK119 (19). In this complex, BAP1 comprises the catalytic deubiquitinase and is stabilized by the ASXL1/2/3 proteins in various tissues. Thus, we determined the global levels of H2AK119Ub in human HSPCs with truncated ASXL1 by flow cytometry and detected a global reduction of H2AK119Ub (Fig. 4H), suggesting that the PR-DUB complex exhibits increased deubiquitinating activity in the presence of truncated ASXL1. To exclude the possibility that input heterogeneity in human HSPCs might be driving the difference in global H2AK119Ub abundance, we performed costaining of H2AK119Ub in our engineered HSPCs with established progenitor and lineage-defining surface markers (Supplementary Fig. S6A). Here, we confirmed that H2AK119Ub abundance was reduced within all progenitor compartments, including immature multipotent, granulocyte–monocyte, megakaryocytic–erythroid, as well as lymphoid progenitors (Supplementary Fig. S6B).

To directly determine the enzymatic activity of the PR-DUB complex with either full-length or truncated ASXL1, we produced His-tagged BAP1, His-tagged full-length ASXL1, and His-tagged truncated ASXL1 in 293FT cells and purified these expressed proteins. We then performed a cell-free deubiquitinase activity assay using Ub-AMC, a quenched, fluorescent substrate for ubiquitin proteases (17). In this assay, BAP1 alone had moderate deubiquitinase activity, and the addition of full-length ASXL1 markedly enhanced enzymatic activity (Fig. 4I). However, the complex of truncated ASXL1 and BAP1 retained deubiquitinase activity for an extended period of time, leading to a modest increase in overall deubiquitination (Fig. 4I, right). This is consistent with a recent report showing increased stability of the PR-DUB complex with truncated ASXL1 in cell line models (26). These experiments suggest that truncated ASXL1 leads to a global decrease of H2AK119Ub through increased activity of the PR-DUB complex.

Truncated ASXL1 Phenotypes Are Dependent on BAP1

Next, we reasoned that if truncated ASXL1 exerts its functional effects through the PR-DUB complex, then the removal of BAP1 should disrupt these phenotypes. To investigate this possibility, we took advantage of the fact that the K562 leukemia cell line harbors an endogenous ASXL1 nonsense mutation (Y591*). We used CRISPR/Cas9 to revert the K562 ASXL1-mutant allele to wild-type (Supplementary Fig. S7A) and generated single-cell–derived clones with the corrected genotype, as well as single-cell–derived clones with the parental (mutant) genotype. Previous studies on this cell line have associated immature GATA motif accessibility with surface expression of CD24 (28, 29), which we leveraged as a surrogate parameter in these studies. Similar to $CD34^+$ HSPCs, K562 cells carrying the ASXL1 mutation showed decreased H2AK119Ub levels and increased expression of CD24 compared with the corrected cells (Supplementary Fig. S7B). To now investigate the effect of different expression levels of BAP1, we established a CRISPR/Cas9-based approach to delete BAP1 in these cells (Supplementary Fig. S7C and S7D) and a lentiviral vector overexpressing BAP1 (Supplementary Figs. S7E and S7F). Using these methods, we generated BAP1 KO and BAP1 overexpression clones on the background of ASXL1-mutant or ASXL1-wild-type K562 cell lines (Fig. 4J; Supplementary Fig. S7G). Using CD24 as a surrogate immature marker, we observed that expression of CD24 was abrogated upon deletion of BAP1 and enhanced upon BAP1 overexpression but only in the context of mutant ASXL1 (Fig. 4K and L). Thus, these data demonstrate that BAP1 is necessary to induce CD24 expression in the K562 cell line.

Next, we utilized multiplexed gene engineering to simultaneously introduce both the ASXL1 truncation and deletion of BAP1 into $CD34^+$ HSPCs (Fig. 4M) and transplanted these double-mutant cells into NSGS mice ($n = 5$). At 8 weeks, engraftment was overall low, in line with previous observations that BAP1 is important for HSC function (Fig. 4N;

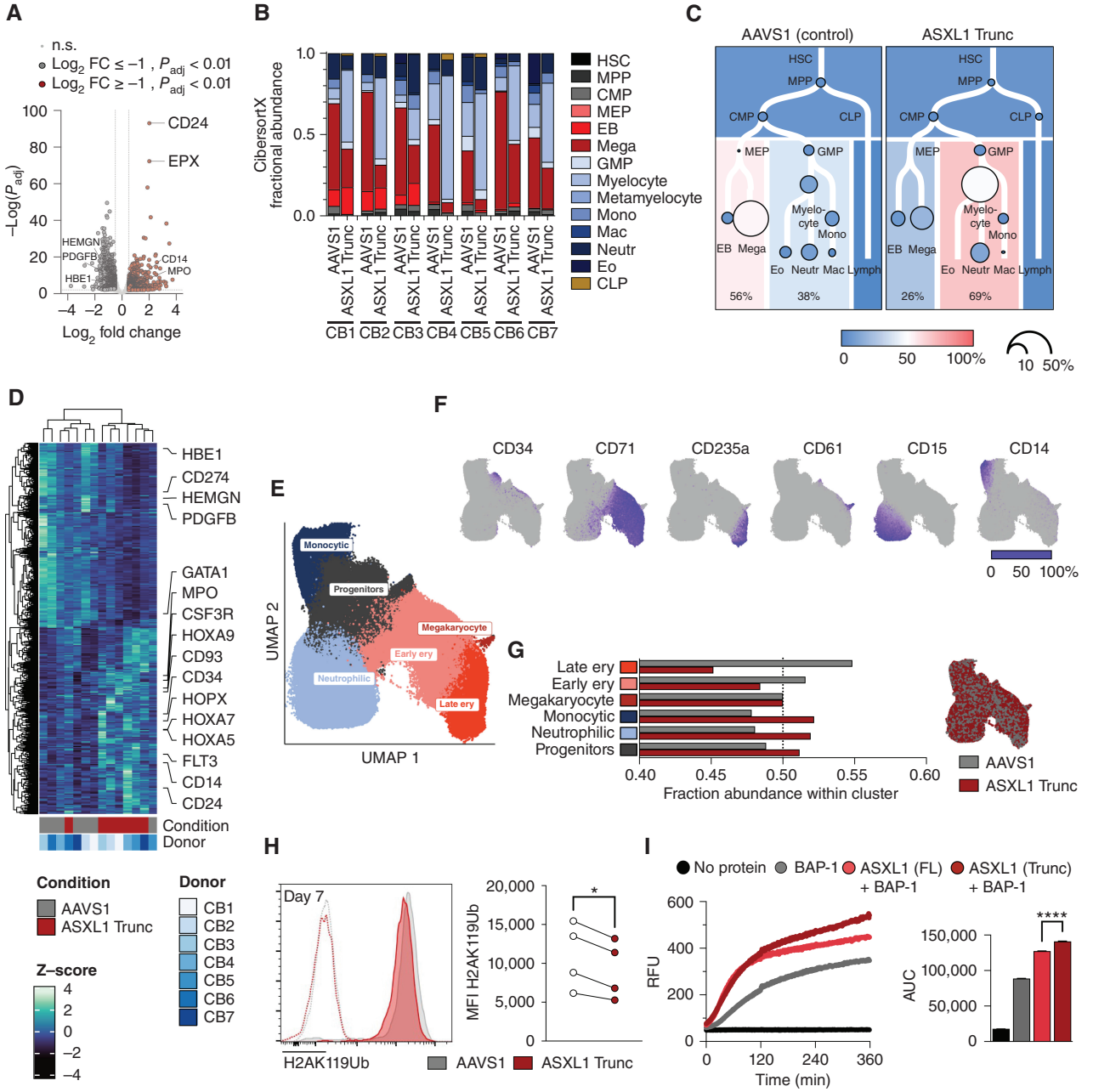

Figure 4. Truncating ASXL1 mutations are associated with the activation of myeloid transcriptional programs and global reduction of H2AK119Ub through the PR-DUB complex. **A,** Volcano plot of RNA-seq from engineered, cord-blood–derived HSPCs comparing AAVS1 control and ASXL1 Trunc cells ($n = 7$ cord-blood donors). Gray circles with black border: genes upregulated in AAVS1 control relative to ASXL1 Trunc, $P_{adj} < 0.01$, $Log_2(FC) < -1$. Red circles: genes upregulated in ASXL1 Trunc relative to AAVS1, $P_{adj} < 0.01$, $Log_2(FC) > 1$; n.s. = not significant. **B,** CIBERSORTx fractions of digitally deconvoluted RNA-seq profiles from HSPCs with either AAVS1 control or ASXL1 Trunc editing. **C,** Average CIBERSORTx fractional abundance in AAVS1 control (left) or ASXL1 Trunc (right) HSPCs. **D,** Heat map of gene-expression levels in genes significantly dysregulated between AAVS1 control and ASXL1 Trunc HSPCs ($P_{adj} < 0.05$). **E,** Clustered UMAP of 21-parameter flow cytometry on engineered HSPCs 7 days after engineering in pan-differentiation media (StemSpan with SCF, FLT3-L, EPO, TPO, IL3, IL6, IL9, GM-CSF, and G-CSF). **F,** Heat maps of relevant hematopoietic differentiation markers CD34, CD71, CD235a (GPA), CD61, CD15, and CD14. **G,** Relative abundance of either AAVS control (gray bars) or ASXL1 Trunc cells (red bars) within each cluster (left) and UMAP colored by condition (right). **H,** H2AK119Ub by intracellular flow cytometry in HSPCs 7 days after CRISPR/Cas9-engineering. Representative histogram (left; dotted lines: isotype control staining, solid lines: H2AK119Ub staining); mean fluorescence intensity (MFI) of 4 independent donors (right); statistical significance was determined by the Student *t* test. **I,** Cell-free deubiquitinase activity assay using Ub-AMC as substrate with either no protein (black), purified BAP1 alone (gray), BAP1 with full-length ASXL1 (light red), or BAP with truncated ASXL1 (dark red) over time (left; average of $n = 2$ independent experiments). Area under the curve (AUC) for each condition (right); statistical significance was determined by the Student *t* test.
(*continued on following page*)

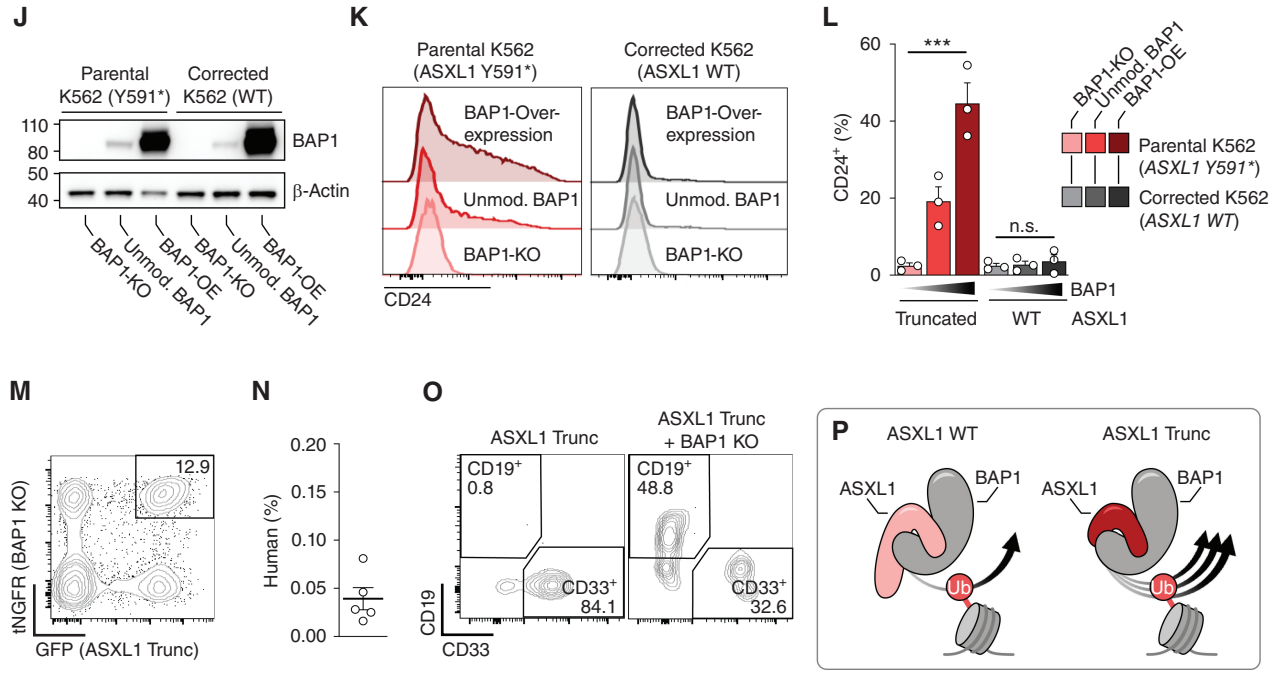

Figure 4. ***(Continued)*** **J,** Western blot analysis of isogenic K562 cell lines with parental (ASXL1 Y591*) or corrected (ASXL1 WT) genotype with either BAP1 deletion, unmodified BAP1, or BAP1 overexpression. **K,** CD24 expression in isogenic K562 cell lines with either BAP1 deletion (BAP1 KO), unmodified BAP1, or BAP1 overexpression. **L,** Percentage of CD24+ cells in isogenic K562 cell lines with either BAP1 deletion (BAP1 KO), unmodified BAP1, or BAP1 overexpression. $n = 3$ biological replicates for each genotype derived from separate, single-cell–derived clones. Statistical significance was determined by the Student t test. **M,** Flow cytometry of multiplex editing in CD34+ HSPCs for ASXL1 Trunc (GFP) and BAP1 deletion (expressing truncated NGFR receptor). **N,** Engraftment of human hCD45+ cells in mouse bone marrow of NSGS mice engrafted with ASXL1Trunc/BAP1KO cells ($n = 5$). **O,** Representative flow cytometry plots for lineage distribution from mice engrafted with either ASXL1 Trunc alone (left) or ASXL1 Trunc/BAP1 KO multiplex engineered cells. **P,** Schematic of PR-DUB activity with wild-type (left) or truncated ASXL1 (right). Arrows denote deubiquitinase activity. *, $P < 0.05$; ***, $P < 0.001$; ****, $P < 0.0001$.

ref. 30). However, we did observe the rescue of the lymphoid potential of the double-mutant cells, suggesting that the myeloid skewing observed in HSPCs with truncated ASXL1 alone is dependent on BAP1 (Fig. 4O). Taken together, these results suggest that truncated ASXL1 is dependent on the presence of BAP1 to exert phenotypic changes in hematopoietic cells through increased deubiquitinase activity of the protein complex (Fig. 4P).

Truncating ASXL1 Mutations Lead to a Global Redistribution of H2AK119Ub

Given that truncating ASXL1 mutations lead to a global reduction in H2AK119Ub, we next examined the genome-wide distribution of H2AK119Ub in these engineered HSPCs using Cleavage Under Targets and Release Using Nuclease (CUT&RUN) chromatin sequencing (31). Similar to our observations by flow cytometry, the median occupancy of H2AK119Ub across the mappable genome was reduced in cells with truncated ASXL1 (Fig. 5A). However, because the H2AK119Ub occupancy is variable across the genome (Fig. 5B), we next aimed to perform a more detailed characterization of the changes in H2AK119Ub occupancy in cells with truncated ASXL1.

Overall, H2AK119Ub is prevalent across the entire genome, dominated by kilo- to megabase-sized domains of high occupancy, whereas low levels of H2AK119Ub can be detected very broadly (32). In line with a global reduction of H2AK119Ub in cells with truncated ASXL1, we observed a reduction in these broad low-occupancy areas, but intriguingly, we found an increase of H2AK119Ub in high-occupancy regions, as exemplified by the HOXA cluster (Fig. 5C). To systematically characterize these relationships, we plotted the occupancy of H2AK119Ub along 10 kb–sized bins across the entire genome (Fig. 5D). Here, we note that although H2AK119Ub occupancy is highly correlated between AAVS1 control and ASXL1 Trunc HSPCs, the slope of the relationship is >1. This observation suggests that in human HSPCs, areas of high H2AK119Ub occupancy are further enriched, whereas low-occupancy regions are further depleted with truncated ASXL1. Focusing on bins with significantly differential H2AK119Ub occupancy, we indeed see that those bins significantly enriched in ASXL1 Trunc HSPCs have significantly higher H2AK119Ub occupancy, whereas bins significantly enriched in AAVS1 controls HSPCs have lower H2AK119Ub occupancy (Fig. 5D, right). Taken together, our data from engineered human HSPCs suggest that in cells with truncated ASXL1, H2AK119Ub occupancy in high-occupancy bins increases, whereas in low-occupancy bins, it decreases (Fig. 5E). To further explore whether this phenomenon holds true beyond human HSPCs, we profiled H2AK119Ub both in our isogenic K562 cell line system (Supplementary Fig. S8A) as well as in primary human AML blasts sorted from patients with ($n = 3$) or without ($n = 4$) mutations in ASXL1 (Supplementary Fig. S8B and S8C). Here, we observed the same

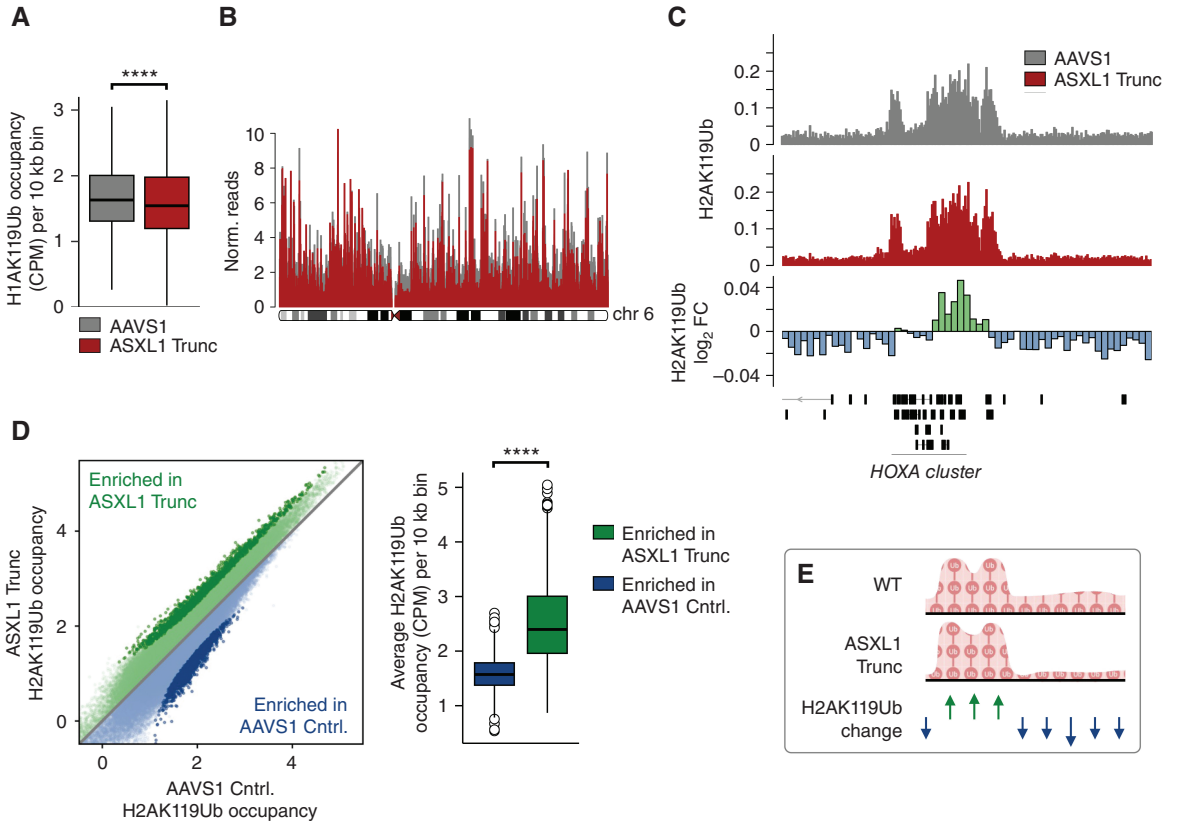

Figure 5. Truncating ASXL1 mutations are associated with a global redistribution of H2AK119Ub and increased transposase-accessible chromatin. **A,** Comparison of H2AK119Ub occupancy between AAVS1 control (gray) and ASXL1 Trunc (red) HSPCs per 10 kb bin across the genome. **B,** Overview depicting H2AK119Ub occupancy across chromosome 6 in edited AAVS1 control (gray) and ASXL1 Trunc (red) HSPCs. **C,** Representative H2AK119Ub-enriched domains at the *HOXA* locus on chromosome 7 showing genome tracks for H2AK119Ub occupancy and H2AK119Ub $\log_2$ fold change. **D,** Normalized H2AK119Ub occupancy per 10 kb bins across the genome between AAVS1 control (*x*-axis) and ASXL1 truncated (*y*-axis) HSPCs, depicted as $\log_2$ CPM (left), with dark green and dark blue denoting significantly ($P < 0.05$) occupied bins as determined by empirical Bayes quasi-likelihood F-tests. Average H2AK119Ub occupancy for bins with significantly differential H2AK119Ub occupancy enriched in AAVS1 control (blue) or ASXL1 Trunc (green) HSPCs; statistical significance was determined by the Student *t* test. **E,** Schematic depicting the observed relationship of H2AK119Ub occupancy changes upon truncation of ASXL1. (*continued on following page*)

pattern: samples with ASXL1 mutations showed relative increases of H2AK119Ub in high-occupancy regions and relative decreases in low-occupancy regions. Furthermore, this relationship was also detectable in a published data set from patients with chronic myelomonocytic leukemia (CMML; ref. 33), again showing that bins with high H2AK119Ub occupancy are further enriched, whereas low-occupancy regions are further depleted in samples with mutant ASXL1 (Supplementary Fig. S8D).

Finally, we interrogated publicly available data sets in which PR-DUB activity is reduced; here, the opposite pattern is observed: H2AK119Ub can be seen to accumulate broadly, with low-occupancy bins increasing and high-occupancy bins decreasing (Supplementary Fig. S8E and S8F).

These observations are in line with an emerging understanding of the global role of PR-DUB, which is thought to constrain the pervasive accumulation of H2AK119Ub across the genome (32), with broad accumulation of H2AK119Ub when PR-DUB activity is reduced. This model suggests a dynamic balance of H2AK119Ub deposition (by the PRC1 complex) and removal (by the PR-DUB complex). Several studies have suggested that deletion of PR-DUB leads to broad, low-level accumulation of H2AK119Ub across the genome and is accompanied by redistribution of PRC1 away from its core target loci, ultimately leading to paradoxical reduction of H2AK119Ub at high-occupancy regions.

Taken together, our data on the global distribution of H2AK119Ub in human HSPCs with truncated ASXL1 are consistent with a hyperactive PR-DUB, with increased concentration of the histone mark in high-occupancy regions and a further reduction in low-occupancy bins, further confirming that PR-DUB activity is enhanced and not depleted when ASXL1 is truncated. Importantly, we demonstrate that this pattern is not restricted to our experimental system but can be observed in multiple settings, including patient samples from AML (our data) as well as CMML (33).

To characterize the relevance of these changes further, we used Assay for Transposase-Accessible Chromatin with sequencing (ATAC-seq), along with our RNA-seq, and correlated these modalities with H2AK119Ub occupancy. First, we interrogated the overlap of H2AK119Ub domains for AAVS1 control and ASXL1 Trunc HSPCs. In line with a global

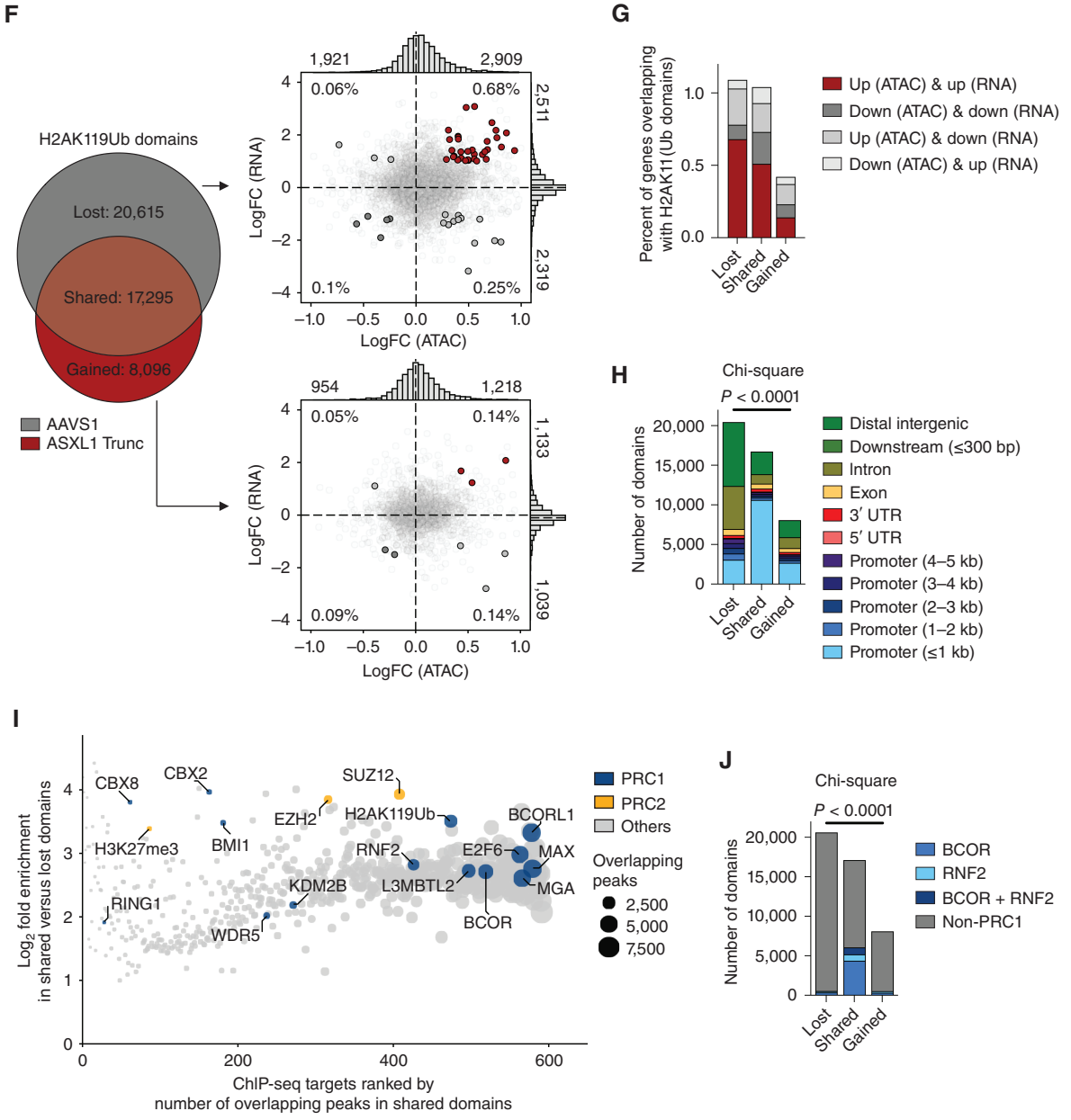

Figure 5. ***(Continued)*** **F,** Number and overlap of H2AK119Ub domains identified in edited AAVS1 control (gray) or ASXL1 Trunc (red) HSPCs (left). Log_2 fold change for ATAC-seq (*x*-axis) and RNA-seq (*y*-axis) per gene overlapping with lost (top right) or gained H2AK119Ub domains (bottom right). Annotated are the number of genes associated with increased/decreased accessibility (horizontal histogram) as well as up-/downregulated expression (vertical histogram). Genes with significant ($P < 0.1$) differential regulation in each of the four quadrants are highlighted, and the percentage of genes as a fraction of all genes associated with the H2AK119Ub domain is denoted for each quadrant [red = up (ATAC) and up (RNA), dark gray = down (ATAC) and down (RNA), mid gray = up (ATAC) and down (RNA), light gray = down (ATAC) and up (RNA)]. **G,** Summary of the percentage of genes overlapping with lost, shared, or gained H2AK119Ub domains with significant ($P < 0.1$) dysregulation by ATAC- and RNA-seq. **H,** Number of H2AK119Ub domains annotated by known functional role in lost, shared, or gained H2AK119Ub domains. Statistical significance determined by the Chi-square test. **I,** Log_2 fold enrichment of chromatin marks and transcription factors in shared versus lost H2AK119Ub domains identified using publicly available ChIP-seq data (35) ranked by the number of overlapping peaks. Members of the PRC1 (blue) and PRC2 (yellow) complexes are highlighted. **J,** Number of domains bound by the PRC1 members BCOR and RNF2 (RING1B) as identified from two additional data sets in K562 (36) and human embryonic stem cells (37). Statistical significance determined by the Chi-square test. ****, $P < 0.0001$.

reduction of H2AK119Ub, fewer domains were detectable in HSPCs with truncated ASXL1 compared with AAVS1 control HSPCs, whereas a considerable number of domains were shared between the conditions (Fig. 5F, left). We then interrogated whether we could observe changes in our ATAC-seq and RNA-seq data for genes within domains that were either lost or gained upon truncation of ASXL1. Here, we saw the highest fraction of genes that showed both increased accessibility by ATAC-seq and upregulation by RNA-seq for genes in H2AK119Ub domains that were lost (Fig. 5F, top

right). Conversely, we observed relatively little changes for both ATAC- and RNA-seq for genes in gained H2AK119Ub domains (Fig. 5F, bottom right). When we quantified these relationships across the three fractions of H2AK119Ub domains (lost, shared, and gained H2AK119Ub), the highest fraction of genes associated with these domains showing increased accessibility and transcriptional upregulation was in lost domains (Fig. 5G), suggesting that loss of H2AK119Ub is associated with increases in transposase-accessible chromatin and transcriptional upregulation.

Next, we performed an integrative pathway enrichment analysis (34) of our multivariate data for genes associated with H2AK119Ub domain loss. Here, we found enrichment of gene sets associated with hematopoietic and leukemic stem cell function (Supplementary Fig. S9A). Of note, further analysis across the three fractions of H2AK119Ub domains (lost, shared, and gained) showed that ATAC-seq and RNA-seq for these gene programs showed the highest correlation in lost H2AK119Ub domains ($P = 0.02$, Supplementary Fig. S9B), and the fraction of upregulated genes associated with these programs was highest in H2AK119Ub lost domains (Supplementary Fig. S9C). Yet, although the members of these gene sets were enriched in domains characterized by H2AK119Ub loss, not all genes were exclusively found in these domains, potentially separating genes that might be directly versus indirectly affected by truncated ASXL1. Taken together, this analysis suggests that H2AK119Ub domain loss in HSPCs with truncated ASXL1 is linked to increased transposase-accessible chromatin and gene expression of established leukemic and hematopoietic stem cell signatures.

Preserved H2AK119Ub Domains Are Highly Enriched for PRC1

In our analysis of H2AK119Ub domains, we noted that a fraction of genes associated with H2AK119Ub domains that were shared between AAVS1 control and ASXL1 truncated HSPCs were associated with differential accessibility and expression (Fig. 5G), leading us to further interrogate the composition of these domains. First, we determined the composition of functional genomic elements within the fractions of H2AK119Ub domains (lost, shared, and gained). Here, we observed that domains that were most frequently lost if ASXL1 is truncated were enriched for intergenic regions, whereas domains that were shared were highly enriched for promoter regions (Fig. 5H). This further suggests that H2AK119Ub loss upon truncation of ASXL1 is not uniform, with intergenic H2AK119Ub being mostly lost, and H2AK119Ub found around promoter regions and gene bodies being preserved. Next, we aimed to interrogate which known chromatin-associated marks are enriched at these shared H2AK119Ub domains. For this purpose, we first interrogated publicly available ChIP-seq data sets (35) and evaluated fold enrichment and number of overlapping peaks of ChIP-peaks (MACS2 Q value $< 1 \times 10^{-5}$) with H2AK119Ub domains shared between AAVS1 and ASXL1 Trunc versus lost H2AK119Ub domains (Fig. 5I). Here, we found strong enrichment for members of the noncanonical PRC1.1 complex such as BCOR and BCORL1, whereas PRC2 members, although enriched, scored lower. To confirm these observations in independent data sets, we extracted targets bound by BCOR and RNF2 (RING1B) for K562 (36) and human embryonic stem cells (37) and overlapped these domains with our data sets. Here, we confirmed a strong enrichment of PRC1 bound loci in H2AK119Ub domains that are preserved upon truncation of ASXL1 (Fig. 5J). Taken together, these observations suggest a concentration of noncanonical PRC1.1 at preserved H2AK119Ub domains in cells with truncated ASXL1, a finding in line with the hyperactivity of PR-DUB.

Hematopoietic Cells with Truncating ASXL1 Mutations Are Vulnerable to PRC1 Inhibition

Given these observations, we asked whether the balance of H2AK119Ub deposition and removal can be exploited therapeutically. First, we investigated how increasing levels of truncated ASXL1 influenced phenotypic changes in hematopoietic cells (Fig. 6A). We generated a doxycycline-inducible vector coexpressing truncated ASXL1 with GFP (Fig. 6B), introduced this vector into our corrected (ASXL1 wild-type) K562 cell lines, and observed increased FLAG-tagged truncated ASXL1 with increasing doses of doxycycline (Fig. 6C; Supplementary Fig. S10A). Correspondingly, we detected a dose-dependent increase in GFP expression coupled with a dose-dependent reduction of global H2AK119Ub (Fig. 6D). We next performed a time- and dose-dependent interrogation of CD24 expression as a surrogate marker of a cell state associated with GATA motif accessibility in K562 cells and found that although GFP expression increased in a time- and dose-dependent matter, the fraction of $CD24^+$ cells initially also increased but

Figure 6. Hematopoietic cells with truncating ASXL1 mutations might be especially vulnerable to PRC1 inhibition. **A,** Schematic depicting the concept of the interplay between H2AK119Ub deposition by the PRC1 complex and removal of H2AK119Ub by the PR-DUB complex (ASXL1/BAP1). In cells with truncated ASXL1, this balance is tilted favoring removal of H2AK119Ub. Here, we investigated how increasing levels of truncated ASXL1 influence phenotypic changes in hematopoietic cells. **B,** Inducible vector-expressing ASXL1:G646fs and GFP under doxycycline-dependent control. **C,** Western blot of anti-FLAG in corrected K562 cells expressing doxycycline-inducible truncated ASXL1, 24 hours after addition of indicated doses of doxycycline. **D,** Flow cytometry of GFP (left) and intracellular staining of H2AK119Ub (right) in cells treated for 24 hours with indicated doses of doxycycline. **E,** Heat map of increasing doses of doxycycline (*x*-axis) and time-course (*y*-axis) depicting GFP MFI (left) and percent $CD24^+$ positive cells (right). **F,** Western blot analysis of H2AK119Ub in K562 cell lines with the indicated genotype 0, 30, and 60 minutes after the addition of 50 μmol/L PRT-4165 to the cell culture. **G,** Viability of parental K562 (ASXL1:Y591*, red) and corrected K562 (ASXL1:WT, gray) 96 hours after addition of the indicated doses of PRT-4165, statistical significance determined by extra sum-of-squares F test. **H,** Western blot for H2AK119Ub, RING1A, RING1B, and Vinculin 24 hours after induction of shRNA-mediated knockdown of the indicated targets genes or shRNA control, respectively. **I,** Viability 96 hours after induction of shRNA-mediated knockdown of the indicated targets normalized to shRNA control, statistical significance determined by Student *t* test. **J,** Colony count and morphologic scoring (500 cells/plate, in triplicate) of engineered cord-blood–derived HSPCs for AAVS1 control and ASXL1 Trunc cells, exposed to 50 μmol/L PRT-4165 for 24 hours prior to plating. Methocult read at 14 days after plating; statistical significance was determined by the Student *t* test. **K,** Viability for primary patient-derived AML blasts from samples without ($n = 7$, left) and with ($n = 5$, middle) mutations in ASXL1 in liquid culture 96 hours after addition of the indicated doses of PRT-4165 (relative to DMSO alone; sample information can be found in Supplementary Fig. S11C) and summary of IC_{50} for samples with IC_{50} estimates (right); statistical significance was determined by the Mann–Whitney test. *, $P < 0.05$; ***, $P < 0.001$; ****, $P < 0.0001$.

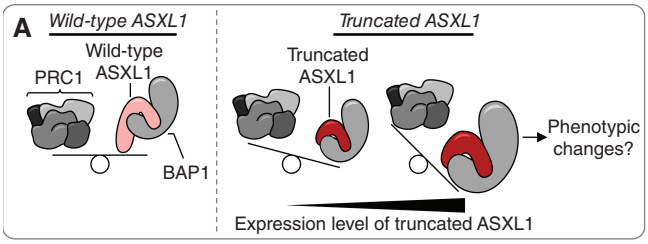
A
Wild-type ASXL1
Truncated ASXL1
Wild-type ASXL1
PRC1
BAP1
Truncated ASXL1
Phenotypic changes?
Expression level of truncated ASXL1

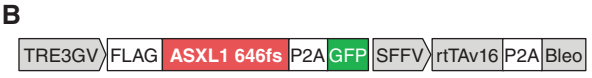
B
TRE3GV
FLAG
ASXL1 646fs
P2A
GFP
SFFV
rtTAv16
P2A
Bleo

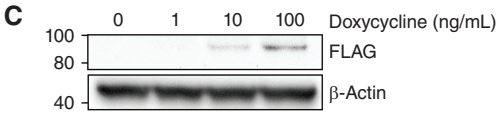
C
0
1
10
100
Doxycycline (ng/mL)
100
80
40
FLAG
β-Actin

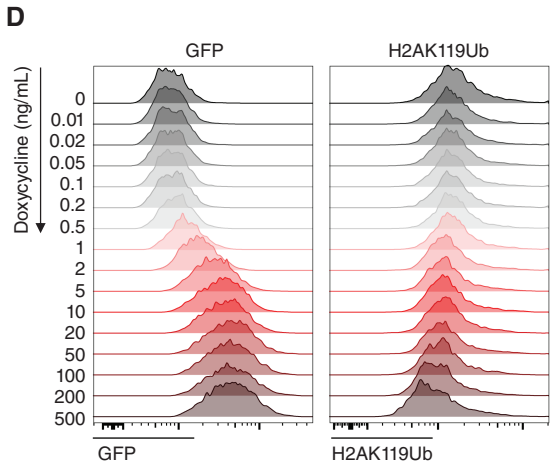
D
GFP
H2AK119Ub
Doxycycline (ng/mL)
0
0.01
0.02
0.05
0.1
0.2
0.5
1
2
5
10
20
50
100
200
500
GFP
H2AK119Ub

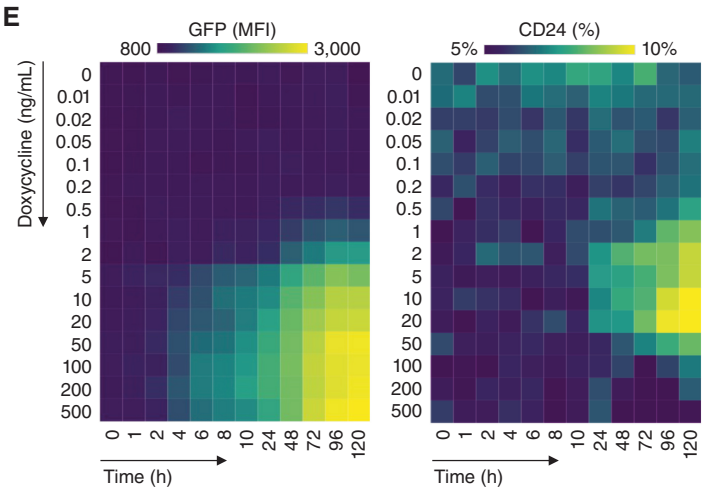
E
GFP (MFI)
800
3,000
CD24 (%)
5%
10%
Doxycycline (ng/mL)
0
0.01
0.02
0.05
0.1
0.2
0.5
1
2
5
10
20
50
100
200
500
0
1
2
4
6
8
10
24
48
72
96
120
Time (h)
Time (h)

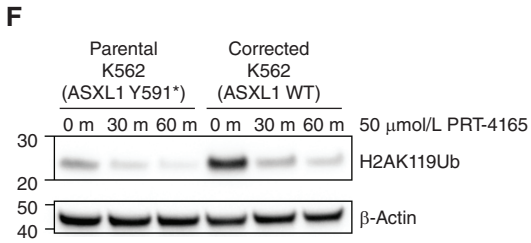
F
Parental K562 (ASXL1 Y591*)
Corrected K562 (ASXL1 WT)
0 m
30 m
60 m
0 m
30 m
60 m
50 μmol/L PRT-4165
30
20
50
40
H2AK119Ub
β-Actin

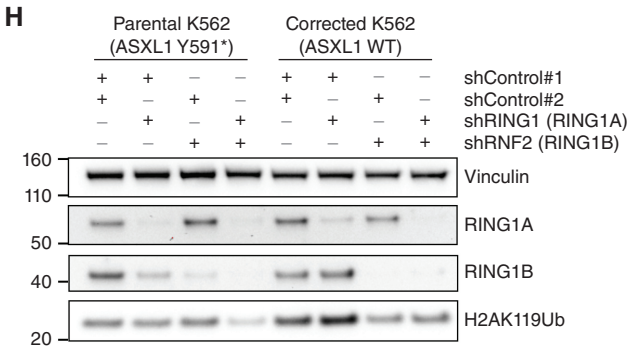
H
Parental K562 (ASXL1 Y591*)
Corrected K562 (ASXL1 WT)
shControl#1
shControl#2
shRING1 (RING1A)
shRNF2 (RING1B)
160
110
50
40
20
Vinculin
RING1A
RING1B
H2AK119Ub

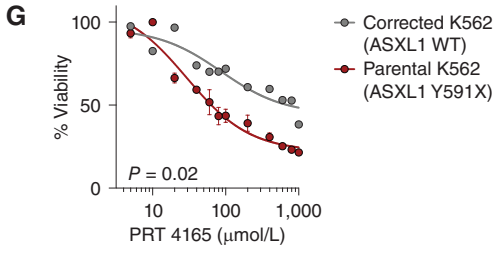
G
100
50
0
% Viability
P = 0.02
10
100
1,000
PRT 4165 (μmol/L)
Corrected K562 (ASXL1 WT)
Parental K562 (ASXL1 Y591X)

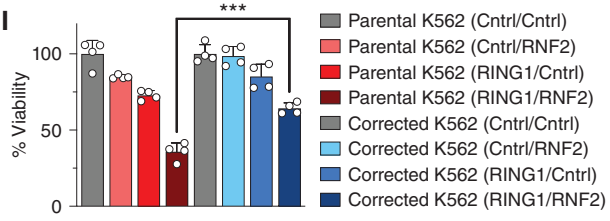
I
***
100
50
0
% Viability
Parental K562 (Cntrl/Cntrl)
Parental K562 (Cntrl/RNF2)
Parental K562 (RING1/Cntrl)
Parental K562 (RING1/RNF2)
Corrected K562 (Cntrl/Cntrl)
Corrected K562 (Cntrl/RNF2)
Corrected K562 (RING1/Cntrl)
Corrected K562 (RING1/RNF2)

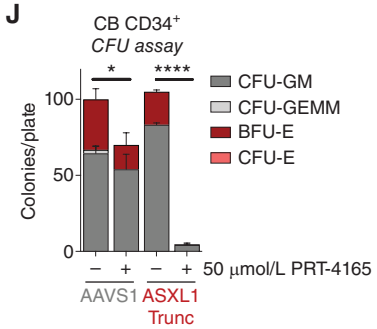
J
CB CD34+
CFU assay
*
****
100
50
0
Colonies/plate
CFU-GM
CFU-GEMM
BFU-E
CFU-E
– + – +
50 μmol/L PRT-4165
AAVS1
ASXL1 Trunc

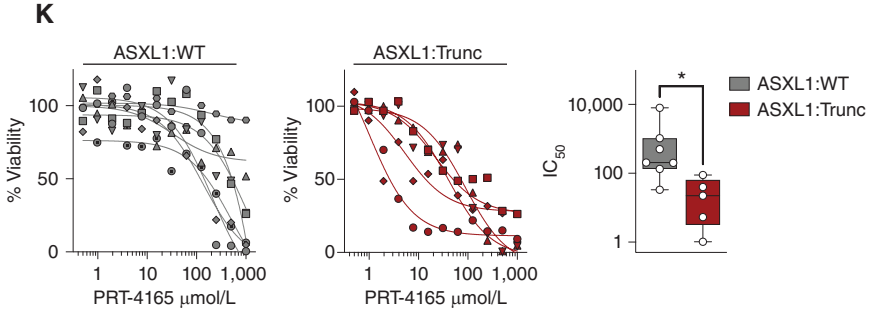
K
ASXL1:WT
ASXL1:Trunc
100
50
0
% Viability
1
10
100
1,000
PRT-4165 μmol/L
10,000
100
1
IC50
*
ASXL1:WT
ASXL1:Trunc

notably dropped off at high doses of doxycycline (Fig. 6E; Supplementary Fig. S10B). This finding suggests that there is a limited range of expression in which truncated ASXL1 and correlated H2AK119Ub reduction show the most profound phenotypes and that further reduction in H2AK119Ub could impair these effects imparted by the expression of truncated ASXL1.

Because (i) H2AK119Ub is deposited by the PRC1 complex for which there are available existing and emerging inhibitors, (ii) PRC1 is highly enriched in preserved H2AK119Ub domains in our sequencing studies, and (iii) our dose-dependent expression of truncated ASXL1 suggested that severely reducing H2AK119Ub shows detrimental effects on the CD24 phenotype in K562 cells, we hypothesized that cells with truncated ASXL1 might be particularly vulnerable to PRC1 inhibition. First, we evaluated the effect of PRC1 inhibition on global levels of H2AK119Ub in cells with either truncated or wild-type ASXL1 and found that cells with truncated ASXL1 had lower levels of H2AK119Ub at baseline and the addition of the PRC1 inhibitor PRT-4165 further decreased these levels (Fig. 6F; Supplementary Fig. S10C). We then evaluated cell viability in our isogenic cell line model. At 96 hours after the addition of PRT-4165, K562 cells with truncated ASXL1 exhibited significantly lower viability compared with K562 cells with wild-type ASXL1 (Fig. 6G). Because PRT-4165 shows poor solubility and bioavailability, we sought to validate the targeting of PRC1 genetically. To achieve this, we performed inducible, shRNA-mediated knockdown of the core PRC1 members RING1A and RING1B in either ASXL1-mutant or ASXL1-wild-type K562 cell lines (Fig. 6H; Supplementary Fig. S11A and S11B). Next, we determined the relative viability 96 hours after induction of knockdown of either RING1A, RING1B, or both. Here, we saw a significant reduction of viability, similar to that observed using PRT-4165 in the context of mutant ASXL1 (Fig. 6I). Taken together, in our isogenic K562 cell line model system, ASXL1-mutant cells show increased vulnerability to PRC1 inhibition.

Next, we interrogated the effect of PRC1 inhibition in primary cells. First, we exposed engineered $CD34^+$ HSPCs to PRT-4165 and investigated their ability to form colonies. Here, we saw a marked reduction in colony formation specifically in cells with truncated ASXL1 (Fig. 6J). Importantly, although we observed a slight reduction of colony formation in AAVS1 control cells exposed to PRT-4165, colony formation was almost completely ablated in the context of truncated ASXL1. Finally, we interrogated the effect of PRC1 inhibition in a set of primary AML patient samples with and without truncating mutations in *ASXL1*. In these experiments, although some expected interpatient variability was observed, we detected increased susceptibility to PRC1 inhibition in AML specimens carrying ASXL1 mutations compared with AML samples lacking such mutations (Fig. 6K, sample information can be found in Supplementary Fig. S11C). In total, we demonstrate that the balance of H2AK119Ub deposition and removal is altered in cells with truncating *ASXL1* mutations and that this balance can be further exacerbated by pharmacologic inhibition of PRC1 leading to cell death. These findings imply that cells and conditions with truncating *ASXL1* mutations might be especially vulnerable to PRC1 inhibition.

DISCUSSION

Mutations in *ASXL1* are frequently found along the entire trajectory of myeloid leukemogenesis, from individuals with CH to patients with overt myeloid disease such as MDS/MPN and AML. However, our understanding of *ASXL1* mutations remains limited, in part because of the lack of representative model systems, and to date, no treatment approaches for blood cancers with mutant ASXL1 have been developed. In this study, we engineered mutations in *ASXL1* directly in primary human HSPCs and characterized their effects on hematopoietic differentiation and leukemogenesis. First, we demonstrated that the location of *ASXL1* mutations is functionally relevant. Specifically, we demonstrated that the introduction of truncating *ASXL1* mutations in the central coding region of the native locus faithfully recapitulates the entire trajectory from CH to lethal myeloid disease, which is not observed with the deletion of the gene. We utilized this model to perform a detailed characterization of the underlying mechanisms. Specifically, we demonstrated that truncating *ASXL1* mutations alter the epigenetic landscape driven by increased activity of the PR-DUB complex and related these changes to increases in transposase-accessible chromatin and gene expression. Finally, we identified a potential therapeutic vulnerability of hematopoietic cells with truncating ASXL1 mutations by inhibition of PRC1. This study contributes to our understanding of the role of ASXL1 mutations in CH and hematologic malignancies and has implications for potential therapeutic strategies.

Mouse models of mutant ASXL1 have contributed to our understanding of the functional relevance of ASXL1 in the hematopoietic system; however, these models have shown conflicting results (11–14, 30). For example, some of these murine model systems have shown a competitive disadvantage for ASXL1-mutant HSPCs (11, 13, 15), whereas others have shown a competitive advantage compared with wild-type cells (12, 14). Thus, only some model systems recapitulate the clinical observations in both CH and myeloid malignancies, where hematopoietic cells with ASXL1 mutations outcompete their wild-type counterparts. The level of ASXL1 expression in the models may be one potential factor contributing to these inconsistencies, with some models showing marked overexpression of the truncated protein compared with endogenous ASXL1 (13–15). Here, we engineer truncated ASXL1 into the endogenous locus with expression directly driven by the native regulatory elements in human HSPCs.

Similarly, functional work performed in cell line systems demonstrated that overexpression of truncated ASXL1 led to the depletion of the H2AK119Ub mark (15, 30), and a recent study confirmed the increased stability of the PR-DUB complex with truncated ASXL1 (26) previously shown by Asada and colleagues (30). These observations are consistent with our finding of increased H2AK119 deubiquitinase activity in primary human cells with truncated ASXL1. Interestingly, Wang and colleagues proposed direct inhibition of BAP1 to ameliorate the phenotypes observed with truncated ASXL1 and identified a potential BAP1 inhibitor from a high-throughput screening library that demonstrated some efficacy in cell lines (26). However, direct pharmacologic inhibition of the PR-DUB complex faces several challenges:

first, the specificity of potential BAP1 inhibitors needs to be examined; second, we and others have demonstrated that deletion of BAP1 in human HSPCs has detrimental effects on HSCs (30), suggesting that activity of the wild-type PR-DUB complex is necessary for normal hematopoiesis; finally, somatic mutations in BAP1 have been identified in a variety of solid malignancies and germline mutations in BAP1 are associated with BAP1 tumor predisposition syndrome (BAP1-TPDS; ref. 38). Individuals with BAP1-TPDS experience increased rates of melanoma, malignant mesothelioma, and renal cell carcinoma (39). Thus, nonspecifically targeting all BAP1 activity is likely to produce significant toxicity, and further work is needed to identify inhibitors that are capable of specifically targeting the PR-DUB complex with truncated ASXL1. Development of such agents is likely to require structural studies of the PR-DUB complex with truncated ASXL1.

Our study is not without limitations. First, efficient gene engineering of primary cord-blood–derived CD34$^+$ HSPCs requires *in vitro* culture of these cells in cytokine-rich media, electroporation with recombinant Cas9, and exposure to rAAV6 viral particles (24). In addition, xenotransplantation of engineered, human HSPCs requires irradiation of the host mice, and engraftment is most efficient in NSGS mice, which express high levels of human cytokines (40). These factors put significant proliferative stress on hematopoietic cells. Although all experiments in our study were performed with AAVS1 edited controls to account for these factors, our approach may accelerate any phenotypes that are induced by proliferative stress. It is therefore likely that differences in proliferation and malignant transformation might show longer latency in environments without these stressors. In addition, in the cases of clonal outgrowth observed in our study, secondary transplantation of these specimens did not yield a fully lethal phenotype, suggesting that secondary genetic lesions might be required for fully penetrant transformation.

Second, H2AK119Ub is one of the most prevalent chromatin marks in the human genome (17), and others have demonstrated that H2AK119Ub is regulated in a highly dynamic manner (20, 41). Performing bulk sequencing to characterize H2AK119Ub occupancy in the most relevant cellular context—primary HSPCs—likely underestimates the cell-to-cell variability of H2AK119Ub occupancy during hematopoietic differentiation. Although technologies to interrogate chromatin marks on very small samples, including single cells, have improved markedly over the past years (42), diffuse repressive marks such as H2AK119Ub face special technical challenges to be scaled down easily. Future iterations of these evolving technologies will likely further improve our understanding of how H2AK119Ub affects cellular phenotypes.

Third, the number of interaction partners that have been identified for the PRC1, PRC2, and PR-DUB complexes is vast. Given the fundamental importance of these protein complexes in regulating the epigenome in many cellular contexts, the complexity of their regulation is not surprising. The PR-DUB complex has been shown to interact with several other proteins outside of BAP1/ASXL1; most notably, BAP1 can interact with ASXL2 and ASXL3, as well as forkhead box K1 and K2 (FOXK1/K2; refs. 19, 20), host cell factor-1 (HCF-1), and O-linked N-acetylglucosamine transferase (OGT; 43), among others. However, the role these other interaction partners play in myeloid leukemogenesis is still being explored, and further studies are required to elucidate the contribution of these additional binding partners of BAP1 to hematopoietic phenotypes.

Notably, an intriguing study by Fujino and colleagues (44) suggested the involvement of the mTOR/AKT pathway in cells expressing truncated ASXL1. This included sensitivity to the mTOR inhibitor sirolimus (rapamycin). However, none of the inhibitors of the mTOR/AKT axis used in the BEAT-AML study (45) showed enhanced sensitivity of ASXL1-mutant cases, suggesting that further investigation of the context in which this pathway might be relevant is needed.

Finally, the available PRC1 inhibitor (PRT-4165) shows poor solubility and bioavailability; thus, it is limited in the extent to which it can be used therapeutically. Specifically, *in vivo* experiments will require more potent and bioavailable inhibitors, which are being developed (46, 47). We envision future studies in which we will be able to interrogate the therapeutic efficacy of this approach further against both CH and myeloid malignancies in *in vivo* models.

Our study systematically explored the role of mutations in ASXL1 on human hematopoiesis and progression into myeloid malignancy. We identified key features relevant to mutant ASXL1 clonal expansion and leukemogenesis and developed a model system using primary human CD34$^+$ HSPCs that faithfully recapitulates the entire spectrum from CH to myeloid disease. We identified potential therapeutic approaches and demonstrated evidence of *in vitro* efficacy in human HSPCs and primary patient AML samples. Our model system and associated findings serve to advance our understanding of ASXL1-mutant leukemogenesis.

METHODS

Primary Human Samples

AML patient samples were obtained from patients with *de novo* AML prior to treatment, with written informed consent in accordance with the Declaration of Helsinki and according to institutional guidelines (Stanford University Institutional Review Board No. 6453). Cord blood was collected with written informed consent from the mother before delivery of full-term pregnancies at the Lucile Packard Children's Hospital through the Stanford Binns Program for Cord Blood Research or purchased from the New York Blood Center. Samples were processed using Ficoll-Paque PLUS (GE Healthcare) density gradient media to isolate mononuclear cells, followed by ACK lysis (ACK Lysing Buffer, Thermo Fisher Scientific) to remove remaining red blood cells. CD34 enrichment was performed by magnetic cell separation using MACS CD34 Microbeads (Miltenyi Biotec).

Cell Sorting of Primary Human AML Samples

Sorting for genotyping assays was performed as previously described (5). Briefly, AML specimens were thawed, washed, stained, and sorted on a FACSAria II SORP (BD). For all genotyping of AML presented here, the "blast" fraction, defined as CD45dim/SSClow, was used as input. Sort purities were acquired for all sorted populations, and purity >99% was required for the blast fraction. For CUT&RUN assays and *in vitro* PRC1 inhibitor assays, blasts were similarly isolated by FACS and then subjected to downstream assays.

Animal Care

Animal experiments were performed with 6- to 8-week-old NOD.Cg-Prkdcscid Il2rgtm1Wjl Tg(CMV-IL3,CSF2,KITLG)1Eav/MloySzJ

(NSGS) mice (Jackson Laboratory). All mouse experiments were conducted in accordance with a protocol approved by the Institutional Animal Care and Use Committee (Stanford Administrative Panel on Laboratory Animal Care #22264) and in adherence with the U.S. NIH's Guide for the Care and Use of Laboratory Animals. Human cells were engrafted 2 to 24 hours after sublethal irradiation (200 rad) by intrafemoral injection of 50,000 to 500,000 cells. Complete blood counts (CBC) were acquired from peripheral blood acquired by tail-vein bleeding on an automated CBC counter (HemaTrue). Bone marrow aspirates were obtained from the transplanted femur for FACS analysis and sorting.

Genotyping

Targeted NGS was performed using commercially available reagents according to the manufacturer's specifications. Briefly, purified genomic DNA was sheared using a Covaris S220 instrument to 250 bp fragments, end repair and adapter ligation were performed using the Celero DNA-seq kit (Tecan Genomics), and hybrid capture was performed using the xGen AML Cancer Panel (IDT). Libraries were sequenced on the Illumina HiSeq platform. Variant calling was performed using an established pipeline in the Majeti Lab as described below. Briefly, after quality control and read trimming using TrimGalore (https://doi.org/10.5281/zenodo.5127899), reads were aligned to the hg38 reference genome using BWA-MEM (48), sorted, indexed, and de-duplicated using SAMTools (49) and Picard (http://broadinstitute.github.io/picard), respectively. Variants were called using Mutect2 (50), VarScan2 (51), and VarDict (52) in parallel. Only variants called by ≥2 callers were retained and annotated using SnpEff (53). Libraries for previously genotyped cohorts were prepared and processed as described previously (54, 55), and genotyping calls were integrated with our current cohort. Oncoprint and comutation plots were generated using Maftools (56). Fishplots were generated using fishplot for R (57). Circos plot was generated using shinyCircos for R (58).

CRISPR/Cas9 Genome Engineering of Primary HSPCs

CRISPR/Cas9 nucleofection was performed as previously described (59). Synthetic, chemically modified sgRNAs and Cas9 protein (Alt-R HiFi CRISPR-Cas9) were purchased from IDT (sgRNA sequences are listed in Supplementary Table S3). Cas9 protein was precomplexed with sgRNA at a molar ratio of 1:2.5 at 25°C for 10 minutes immediately prior to electroporation into $CD34^+$ cells. $CD34^+$ HSPCs were electroporated 2 days after isolation using the Lonza Nucleofector 4D (program EO-100) at 5×10^6 cells/mL in P3 buffer and 150 μg/mL Cas9 protein. For experiments without the use of homology-directed repair (HDR), editing efficiency was determined by amplicon sequencing via NGS at the indicated time points. For experiments presented in Fig. 1, 200 bp amplicons surrounding the putative cut site were generated, amplified from genomic DNA separately, and pooled before sequencing (primer sequences utilized are listed in Supplementary Table S3). Data were analyzed using CRISPResso2 (60) in pooled mode. For experiments requiring rAAV6 donors for HDR, AAV vector plasmids were cloned in the pAAV-MCS plasmid (Agilent Technologies) containing inverted terminal repeat (ITR) sequences from AAV serotype 2 (AAV2). The homology arms for HDR donors were 400 base pairs. rAAV6 vectors were produced in HEK293FT cells transfected using polyethylenimine with 6 μg ITR-containing plasmid and 22 μg pDGM6 containing the AAV6 cap genes, AAV2 rep genes, and adenovirus five helper genes. rAAV6 was harvested using the AAVpro Purification Kit (Takara Bio Inc.) according to the manufacturer's instructions and then stored at –80°C until further use. Following electroporation, cells were incubated for 15 minutes at 37°C, after which rAAV6 donor vectors were added at a multiplicity of infection of 50,000 vector genomes/cell. After 6 hours, media were exchanged, and cells were incubated for 72 hours before purification by FACS. CRISPR/Cas9-mediated correction of the endogenous ASXL1 mutation (Y591*) in K562 cells was performed with some modifications, specifically a sgRNA was designed to target the Y591* allele (Supplementary Table S3), electroporation was performed in Opti-MEM using program FF-120, and the HDR template (Supplementary Table S3) was electroporated alongside the Cas9/sgRNA complex as a single-stranded oligo of 112 bp length.

Cell Culture

$CD34^+$ HSPCs were cultured in low-density conditions (≤200,000 cells/mL), low oxygen conditions (5% O_2), in StemSpan SFEM II (STEMCELL Technologies) base media supplemented with 100 ng/mL of TPO, SCF, FLT3L, IL6 (PeproTech), and the small-molecule UM-171 (35 nmol/L). K562 cells were cultured in IMDM supplemented with 10% FBS and tested regularly for the absence of *Mycoplasma* (MycoAlert Mycoplasma Detection Kit, Lonza).

In Vitro *Differentiation Assays*

For erythroid differentiation assays, $CD34^+$ HSPCs were plated in StemSpan SFEM II supplemented with 1× StemSpan Erythroid Expansion Supplement (STEMCELL Technologies) and 1× penicillin–streptomycin (P/S, Gibco). For myeloid differentiation assays, $CD34^+$ HSPCs were plated in Myelocult H5100 (STEMCELL Technologies) supplemented with SCF, FLT3L, IL3, IL6, GM-CSF, G-CSF (all 20 ng/mL, PeproTech), 0.5 μg/mL Hydrocortisone, and 1× P/S. For megakaryocyte differentiation assays, $CD34^+$ HSPCs were plated in StemSpan SFEM II supplemented with human low-density lipoproteins and 1× Megakaryocyte Expansion Supplement (STEMCELL Technologies). For stem retention assays, cells were cultured in SFEM II (STEMCELL Technologies) base media supplemented with 100 ng/mL of TPO, SCF, FLT3 L (PeproTech), and the small-molecule UM-171 (35 nmol/L). For colony formation assays, 1,500 $CD34^+$ HSPCs were added to 4 mL of MethoCult H4435 (STEMCELL Technologies) and plated in triplicate (500 sorted cells/plate). The number of colonies in each sample was scored at 12 to 16 days by morphology or imaged using the StemVision MethoCult imaging system. Surface area in composite images was quantified using Fiji (61). For replating assays, cells were washed and replated 100,000 cells/plate. For pan-differentiation media, cells were cultured in StemSpan SFEM II supplemented with 0.05× StemSpan Erythroid Expansion Supplement, 1× Megakaryocyte Expansion Supplement (all STEMCELL Technologies), SCF, FLT3L, IL3, IL6, GM-CSF, G-CSF (all 20 ng/mL, PeproTech), 0.5 μg/mL Hydrocortisone, and 1× P/S. Liquid differentiation assays were read out by flow cytometry using either a FACSAria II SORP or FACSymphony A5 system with appropriate antibody staining as indicated. For pan-differentiation assay (Fig. 4E–G), cells were stained with a 21-color panel (Supplementary Table S4), data were analyzed using FlowJo v10.8 Software (BD Life Sciences), and UMAPs were plotted using ggplot2 for R (62).

Engraftment Analysis

For engraftment analysis of xenograft mice, red blood cells from bone marrow aspirates or mouse tissue after sacrifice were removed using ACK lysis (ACK Lysing Buffer, Thermo Fisher Scientific) and subsequently stained for lineage markers (Supplementary Table S4). Cells were analyzed by FACS, and human cells were sorted for subsequent analysis. For histologic analysis, tissue specimens were fixed in 10% paraformaldehyde for 48 hours. Bone specimens were decalcified in 0.5 mol/L EDTA for 1 week at 4°C, followed by paraffin embedding, sectioning, and H&E staining. IHC was performed using anti-CD45 (Cell Signaling Technology, cat no. 13917, RRID:AB_2750898), biotin-conjugated anti-Rabbit secondary antibody (Thermo Fisher Scientific, cat no. 31820, RRID:AB_228340), VECTASTAIN Elite ABC (Avidin–Biotin Complex) Kit, and DAB Peroxidase substrate kit (both

from Vector Labs). For cytospin analysis, 20,000 sorted cells/mL were resuspended in PBS with 0.1% bovine serum albumin and cytospun onto slides, followed by methanol fixation and standard May–Grünwald–Giemsa staining.

Western Blot

For Western blot analysis, cells were lysed with M-PER lysis reagent (Thermo Fisher), supplemented with DNase (Worthington Biochemical) and Roche EDTA-free cOmplete Protease Inhibitor. After SDS-polyacrylamide gel electrophoresis (NuPAGE 4%–12% Bis-Tris Gel, Invitrogen), proteins were transferred onto 0.45-μm nitrocellulose membranes (Amersham Protan, GE Healthcare Life Sciences). Primary antibodies utilized were anti–C-term.-ASXL1 (D1B6V), anti–HA-Tag (C29F4), anti–β-actin (8H10D10), anti–H2AK119Ub (D27C4), anti–DYKDDDDK-Tag, anti-Ring1A (D2P4D), anti-RING1B (D22F2; all Cell Signaling Technologies), anti-BAP1 (cat. C15200212, Diagenode), anti–N-Term.-ASXL1 (6E2, Santa Cruz Biotechnology), and anti-vinculin (V284, Bio-Rad). Secondary antibodies were horseradish peroxidase–conjugated anti-rabbit and anti-mouse (both Cell Signaling Technology). Antibodies were detected using Clarity Western ECL Substrate (Bio-Rad), except for HA-Tag, which was detected using Lumi-Light Western Blotting Substrate (Roche).

Lentivirus Production and PiggyBac Transposon-Based Gene Insertion

The ASXL1:G646fs coding sequence was cloned into the pLVX-IRES-dsRed vector (Takara Bio Inc.), and lentiviral particles were produced in HEK293FT cells transfected using Lipofectamin 3000 (Thermo Fisher). After 48 to 72 hours, K562 cells were transduced using the filtered supernatant of virus-producing cells. For inducible ASXL1:G646fs expression, FLAG-ASXL1:G646fs-P2A-ZsGreen was cloned downstream of a TRE3G promoter into a piggyBac donor vector constitutively expressing rtTAV16 and a Bleomycin-resistance cassette. K562 cells were then electroporated with the resulting construct and PBase helper plasmid, selected with Bleomycin, and used for experiments requiring inducible expression. For inducible shRNA-mediated knockdown experiments, lentiviral vectors encoding doxycycline-inducible shRNAs for RING1A (RING1), RING1B (RNF2), or control (Supplementary Fig. S11A) were purchased from TransOMIC Technologies. Lentiviral particles were packaged in HEK293FT cells and transfected using Lipofectamin 3000 (Thermo Fisher). After 48 to 72 hours, K562 cells were transduced using the filtered supernatant of virus-producing cells and selected with puromycin 24 hours after transduction. Knockdown was induced through the addition of 100 ng/mL doxycycline.

Production of Recombinant BAP1, ASXL1:WT and ASXL1:G646fs, and Ub-AMC Hydrolysis Assay

Human BAP1, ASXL1, and ASXL1:G646fs were N-terminally tagged with 6xHis-tag and cloned into the pLVX-IRES-ZsGreen expression vector. HEK293FT cells were transduced with the resulting plasmid using Lipofectamine 3000. After 36h, MG-132 (Sigma-Aldrich) was added to the culture at a final concentration of 10 μmol/L, and cells were harvested 48 hours after transfection using M-PER lysis reagents (Thermo Fisher) supplemented with 200 U/mL DNase (Worthington Biochemical). Proteins were purified using NEBExpress Ni-NTA Magnetic Beads (NEB) according to the manufacturer's protocol. Protein concentration was measured, and 0.5 nmol/L of each protein was used for ubiquitin-AMC assays. The ubiquitin-AMC deubiquitinase assay was performed as previously described (17). Briefly, purified ubiquitin-AMC (UbiQ), containing quenched 7-amido-4-methylcoumarin (AMC), was dissolved in DMSO at a concentration of 20 mg/mL and then further diluted in H_2O to a final stock concentration of 0.5 mg/mL. For activity assays, proteins were mixed with 1 μmol/L ubiquitin-AMC in 25 mmol/L HEPES pH 7.5, 150 mmol/L NaCl, 5 mmol/L DTT, and 0.05% Tween-20 in a final volume of 10 μL in a 384-well plate and read every 20 seconds on a microplate reader using 380 nm excitation and 460 nm emission wavelengths.

CUT&RUN

CUT&RUN chromatin sequencing for H2AK119Ub on engineered CB-derived HSPCs, isogenic K562 cell lines, and primary human AML blast was performed according to published protocols (63). Primary patient samples were sorted by flow cytometry on blasts by gating on CD45dim/SSClow cells (blast gate). 100,000 cells were washed twice in CUT&RUN wash buffer (20 mmol/L HEPES, 150 mmol/L NaCl, 0.5 mmol/L Spermidine, supplemented with Roche EDTA-free cOmplete Protease Inhibitor). Next, activated Concanavalin A–coated magnetic beads (BioMagPlus Concanavalin A, Bang Laboratories) were added to the cell suspension, and cells were allowed to bind to the beads for 10 minutes at room temperature under gentle agitation. After washing, the cells/bead mixture was resuspended in antibody buffer (consisting of wash buffer supplemented with 0.1% digitonin, 2 mmol/L EDTA, and 0.5% BSA) and H2AK119Ub antibody (Clone D27C4) or IgG control (Clone DA1E, both Cell Signaling Technologies) at a 1:50 dilution and incubated with gentle agitation at 4°C overnight. After washing twice to remove unbound antibody, protein A/G-MNase fusion protein (Epicypher) was added to the cell/bead mixture and allowed to bind for 1 hour at 4°C. Cells were washed twice to remove unbound antibodies, resuspended in wash buffer supplemented with 0.1% digitonin, and allowed to cool to 0°C in a chilled ice block before adding $CaCl_2$ to a final concentration of 2 mmol/L to initiate cleavage. After 30 minutes, the reaction was quenched with EDTA and EGTA, and cleaved fragments were allowed to be released into the supernatant by incubating the cells at 37°C for 30 minutes. Fragments were cleaned up using Monarch PCR and DNA Cleanup Kit (NEB), and sequencing libraries were prepared using the Ovation Ultralow V2 DNA-seq Library Preparation Kit (Tecan) according to the manufacturer's protocol and sequenced on the Illumina HiSeq or NovaSeq platforms. After quality control and read trimming using TrimGalore (https://doi.org/10.5281/zenodo.5127899), reads were aligned to the GRCh38 reference genome using bowtie2 (64) using the following settings: –dovetail –very-sensitive –local –no-unal –no-mixed –no-discordant –phred33 -I 10 -X 2000. Alignment was converted to bam format, sorted, and indexed using SAMTools (49) and Picard (http://broadinstitute.github.io/picard). H2AK119Ub domains were identified from CUT&RUN data sets using SEACR (65) in "stringent" mode with default settings. Regions were called for all samples separately and then merged. Occupancy in H2AK119Ub domains was quantified and analyzed using csaw and edgeR for R (66, 67). Heat maps and profile plots were generated using deeptools2 (68), domain overlap and annotation were performed using ChIPpeakAnno (69), and integrated pathway analysis was performed using ActivePathways (34) and (bioRxiv 2023.09.23.559116). Enrichment analysis from published ChIP-seq data sets was performed through the ChIP-Atlas web portal (35). Uniformly processed aligned reads as well as peak calls from published data sets for BCOR and RNF2 (RING1B) and human embryonic stem cells (36, 37) as well as H2AK119Ub for CMML (33), Bap1 KO in murine embryonic stem cells (41), and Asxl2 KO in murine embryonic stem cells (70) were downloaded from the ChIP-Atlas portal (35).

RNA-seq

RNA was isolated from 100,000 engineered CB-derived HSPCs using RNeasy Kits and library preparation, and RNA-seq was performed at the Novogene commercial sequencing facility using standard protocols. Specifically, mRNA was purified using oligo(dT)

coupled magnetic beads, and first-strand cDNA synthesis was performed using random hexamers followed by second-strand cDNA synthesis, end repair, A-tailing, adapter ligation, size selection, amplification, and sequencing on the Illumina HiSeq or NovaSeq platforms. Reads were trimmed and quality control was performed using TrimGalore (https://doi.org/10.5281/zenodo.5127899). The cDNA index was built using Kallisto Bustools (71) using gene annotations downloaded from Ensembl (release 104) and the GRCh38 reference genome. Pseudo-alignment was performed using Kallisto (72). Data were imported into R using tximport (73) using gene mode for analyses presented in Fig. 4 (including Volcano plot, heat map, and quantification of fractional abundance using CIBERSORTx) and in transcript mode for analyses presented in Fig. 5 (correlation to H2AK119Ub occupancy). Differential testing was performed using DESeq2 (74) with cord-blood donor as cofactor and FDR (Benjamini–Hochberg) correction for P values (P_{adj}). Heat maps were generated using ComplexHeatmap (75). CIBERSORTx (27) fractions of digitally deconvoluted RNA-seq profiles were generated by first creating a signature matrix from publicly available RNA-seq profiles of highly purified, hematopoietic progenitors from the Blueprint Consortium (www.blueprint-epigenome.eu) using default settings in the CIBERSORTx matrix generation module (https://cibersortx.stanford.edu/). Then, using the resulting signature matrix (Supplementary Table S5), fractional abundances were determined using the expression values obtained from our engineered CB-derived HSPCs.

ATAC-seq

ATAC-seq libraries from engineered CB-derived HSPCs were prepared as previously described (76). Briefly, 5,000 to 50,000 cells were washed in FACS buffer at 4°C and spun down. Cell pellets were then resuspended in 50 μL of ATAC-seq resuspension buffer (RSB: 10 mmol/L Tris-HCl pH 7.4, 10 mmol/L NaCl, and 3 mmol/L $MgCl_2$ in water) with 0.1% NP40, 0.01% digitonin, and 0.1% Tween-20 and incubated on ice for three minutes. After lysis, 1 mL of ATAC-seq RSB with 0.1% Tween-20 was added, and tubes were inverted six times to mix. Isolated nuclei were then spun down. The supernatant was removed, and nuclei were resuspended in 50 μL transposition mix (25 μL 2× TD buffer, 2.5 μL Tn5 transposase [100 nmol/L final], 16.5 μL PBS, 0.5 μL 1% digitonin, 0.5 μL 10% Tween-20, and 5 μL nuclease-free water). Transposition reactions were incubated at 37°C for 30 minutes in a thermomixer with shaking at 1,000 rpm. Reactions were cleaned up using Qiagen MinElute Reaction Cleanup kits and processed as previously described (76). All libraries were amplified with a target concentration of 20 μL at 4 nmol/L, which is equivalent to 80 femtomoles of product, and sequenced on the Illumina HiSeq or NovaSeq platforms. Data analysis was performed as follows: Read trimming and quality control were performed using TrimGalore (https://doi.org/10.5281/zenodo.5127899) and reads were aligned to the GRCh38 reference genome using bowtie2 (64) and the –very-sensitive option. Aligned reads were converted to bam format, sorted, deduplicated, mitochondrial reads removed, and indexed using SAMTools (49) and Picard (http://broadinstitute.github.io/picard). ATAC-seq reads at TSSs were quantified and differential testing was performed using csaw and edgeR for R (66, 67).

In Vitro *Drug Experiments*

PRT-4165 was dissolved in DMSO and serially diluted in a culture medium. Cells were seeded at 10,000 cells per well for K562 cell lines and primary patient blast samples in 96-well culture plates with a final volume of 200 μL culture media 24 hours prior to the addition of PRT-4165. PRT-4165 was added on day 1, and cell viability and cell count were determined on day 5 (96 hours after the addition of PRT-4165) by FACS using CountBright absolute counting beads (Invitrogen). For H2AK119Ub Western blot analysis, 50 μmol/L PRT-4165 was added at –60 minutes and –30 minutes to 500,000 K562 cells in growth media before extracting protein for Western blotting. For engineered CB-derived HSPCs, 50 μmol/L PRT-4165 was added to the cells in liquid media 24 hours prior to plating for colony-forming assays. Immediately before transfer to MethoCult H4435 (STEMCELL Technologies) media, cells were washed once with fresh media and then plated in triplicate. The number of colonies and morphology was scored at 14 days after plating by morphology.

Statistical Analysis

Statistical analyses were performed in R version 4.3.1 or Prism10 (GraphPad Software). Paired/unpaired t test was used to define statistical significance (*, $P < 0.05$; **, $P < 0.01$; ***, $P < 0.001$; ****, $P < 0.0001$). Experiments were performed with at least 3 biological replicates, with technical duplicates or triplicates per biological sample unless otherwise noted.

Material Availability

All unique reagents generated in this study are available from the lead contact without restriction.

Data and Code Availability

Sequencing data have been deposited in GEO under accession code GSE190738. This paper does not report original code. Any additional information required to reanalyze the data reported in this paper is available from the lead contact upon request. This study makes use of data generated by the Blueprint Consortium. A full list of the investigators who contributed to the generation of the data is available from www.blueprint-epigenome.eu. Funding for the project was provided by the European Union's Seventh Framework Programme (FP7/2007-2013) under grant agreement no 282510 BLUEPRINT.

Authors' Disclosures

T. Köhnke reports grants from the German Research Foundation, the Leukemia and Lymphoma Special Fellow Career Development Award, and the American Society of Hematology Research Restart Award during the conduct of the study and personal fees from TenSixteen Bio outside the submitted work. R. Majeti reports grants from NIH, Stanford Ludwig Center, Leukemia and Lymphoma Society, Mark Foundation for Cancer Research, Paul G. Allen Frontiers Group, Edward P. Evans Foundation, American Society of Hematology during the conduct of the study; personal fees and other support from Kodikaz Therapeutic Solutions, Orbital Therapeutics, Pheast Therapeutics, and 858 Therapeutics; and other support from Myelogene outside the submitted work. No disclosures were reported by the other authors.

Authors' Contributions

T. Köhnke: Conceptualization, data curation, formal analysis, investigation, visualization, methodology, writing–original draft. **K.A. Nuno:** Investigation, writing–review and editing. **C.C. Alder:** Investigation, writing–review and editing. **E.J. Gars:** Investigation, writing–review and editing. **P. Phan:** Data curation, investigation, writing–review and editing. **A.C. Fan:** Formal analysis, investigation, writing–review and editing. **R. Majeti:** Conceptualization, resources, supervision, funding acquisition, writing–original draft, project administration.

Acknowledgments

We would like to thank all patients and their families for providing AML specimens for this study. We thank the donors and their families, as well as the New York Blood Center and the Stanford

Binns Program for Cord Blood Research, for providing cord-blood specimens. We thank Melissa Stafford and the Stanford Veterinary Service Center for animal husbandry services. We thank the Flow Cytometry core at the Stanford Institute for Stem Cell Biology and Regenerative Medicine for providing flow cytometry training, equipment, and support. We thank Agnieszka Czechowicz and members of her lab for providing access to the StemVision Methocult imaging equipment. The Stanford Animal Histology Services (AHS) provided paraffin embedding, sectioning, and H&E staining services. The Stanford Genomics Service Center provided equipment and services used for targeted genotyping library preparation. Some of the computing for this project was performed on the Sherlock cluster, and we thank Stanford University and the Stanford Research Computing Center for providing computational resources and support that contributed to these research results. We also thank all members of the Majeti Lab for helpful input, comments, and discussion. T. Köhnke acknowledges support from the German Research Foundation (DFG, Grant No. KO 5509/1-1), the American Society of Hematology Research Restart Award, and the Leukemia and Lymphoma Special Fellow Career Development Award (Grant No. 3406-21). This work was supported by NIH grants 1R01HL142637 and 1R01CA251331, the Stanford Ludwig Center for Cancer Stem Cell Research and Medicine, the Blood Cancer Discoveries Grant Program through The Leukemia and Lymphoma Society, The Mark Foundation for Cancer Research, The Paul G. Allen Frontiers Group, as well as the Discovery Research Grant from the EvansMDS initiative of the Edward P. Evans Foundation, all to R. Majeti.

The publication costs of this article were defrayed in part by the payment of publication fees. Therefore, and solely to indicate this fact, this article is hereby marked "advertisement" in accordance with 18 USC section 1734.

Note

Supplementary data for this article are available at Blood Cancer Discovery Online (https://bloodcancerdiscov.aacrjournals.org/).

Received November 13, 2023; revised February 7, 2024; accepted February 9, 2024; published first February 14, 2024.

REFERENCES

1. Sallman DA, Komrokji R, Cluzeau T, Vaupel C, Ali NHA, Lancet J, et al. ASXL1 frameshift mutations drive inferior outcomes in CMML without negative impact in MDS. Blood Cancer J 2017;7:633.
2. Chen T-C, Hou H-A, Chou W-C, Tang J-L, Kuo Y-Y, Chen C-Y, et al. Dynamics of ASXL1 mutation and other associated genetic alterations during disease progression in patients with primary myelodysplastic syndrome. Blood Cancer J 2014;4:e177.
3. Metzeler KH, Becker H, Maharry K, Radmacher MD, Kohlschmidt J, Mrózek K, et al. ASXL1 mutations identify a high-risk subgroup of older patients with primary cytogenetically normal AML within the ELN favorable genetic category. Blood 2011;118:6920–9.
4. Paschka P, Schlenk RF, Gaidzik VI, Herzig JK, Aulitzky T, Bullinger L, et al. ASXL1 mutations in younger adult patients with acute myeloid leukemia: a study of the German-Austrian Acute Myeloid Leukemia Study Group. Haematologica 2015;100:324–30.
5. Corces-Zimmerman MR, Hong W-J, Weissman IL, Medeiros BC, Majeti R. Preleukemic mutations in human acute myeloid leukemia affect epigenetic regulators and persist in remission. Proc Natl Acad Sci 2014;111:2548–53.
6. Shlush LI, Zandi S, Mitchell A, Chen WC, Brandwein JM, Gupta V, et al. Identification of pre-leukaemic haematopoietic stem cells in acute leukaemia. Nature 2014;506:328–33.
7. Jaiswal S, Fontanillas P, Flannick J, Manning A, Grauman PV, Mar BG, et al. Age-related clonal hematopoiesis associated with adverse outcomes. N Engl J Med 2014;371:2488–98.
8. Genovese G, Kähler AK, Handsaker RE, Lindberg J, Rose SA, Bakhoum SF, et al. Clonal hematopoiesis and blood-cancer risk inferred from blood DNA sequence. N Engl J Med 2014;371:2477–87.
9. Xie M, Lu C, Wang J, McLellan MD, Johnson KJ, Wendl MC, et al. Age-related mutations associated with clonal hematopoietic expansion and malignancies. Nat Med 2014;20:1472–8.
10. Schnittger S, Eder C, Jeromin S, Alpermann T, Fasan A, Grossmann V, et al. ASXL1 exon 12 mutations are frequent in AML with intermediate risk karyotype and are independently associated with an adverse outcome. Leukemia 2013;27:82–91.
11. Abdel-Wahab O, Adli M, LaFave LM, Gao J, Hricik T, Shih AH, et al. ASXL1 mutations promote myeloid transformation through loss of PRC2-mediated gene repression. Cancer Cell 2012;22:180–93.
12. Inoue D, Kitaura J, Togami K, Nishimura K, Enomoto Y, Uchida T, et al. Myelodysplastic syndromes are induced by histone methylation–altering ASXL1 mutations. J Clin Invest 2013;123:4627–40.
13. Nagase R, Inoue D, Pastore A, Fujino T, Hou H-A, Yamasaki N, et al. Expression of mutant Asxl1 perturbs hematopoiesis and promotes susceptibility to leukemic transformation. J Exp Med 2018;215:1729–47.
14. Yang H, Kurtenbach S, Guo Y, Lohse I, Durante MA, Li J, et al. Gain of function of ASXL1 truncating protein in the pathogenesis of myeloid malignancies. Blood 2018;131:328–41.
15. Balasubramani A, Larjo A, Bassein JA, Chang X, Hastie RB, Togher SM, et al. Cancer-associated ASXL1 mutations may act as gain-of-function mutations of the ASXL1-BAP1 complex. Nat Commun 2015;6:7307.
16. Hsu Y-C, Chiu Y-C, Lin C-C, Kuo Y-Y, Hou H-A, Tzeng Y-S, et al. The distinct biological implications of Asxl1 mutation and its roles in leukemogenesis revealed by a knock-in mouse model. J Hematol Oncol 2017;10:139.
17. Foglizzo M, Middleton AJ, Burgess AE, Crowther JM, Dobson RCJ, Murphy JM, et al. A bidentate polycomb repressive-deubiquitinase complex is required for efficient activity on nucleosomes. Nat Commun 2018;9:3932.
18. Zhang T, Cooper S, Brockdorff N. The interplay of histone modifications – writers that read. EMBO Rep 2015;16:1467–81.
19. Barbour H, Daou S, Hendzel M, Affar EB. Polycomb group-mediated histone H2A monoubiquitination in epigenome regulation and nuclear processes. Nat Commun 2020;11:5947.
20. Kolovos P, Nishimura K, Sankar A, Sidoli S, Cloos PA, Helin K, et al. PR-DUB maintains the expression of critical genes through FOXK1/2- and ASXL1/2/3-dependent recruitment to chromatin and H2AK119ub1 deubiquitination. Genome Res 2020;30:1119–30.
21. Micol J-B, Abdel-Wahab O. The role of additional sex combs-like proteins in cancer. Cold Spring Harb Perspect Med 2016;6:a026526.
22. Hoischen A, van Bon BW, Rodríguez-Santiago B, Gilissen C, Vissers LE, de Vries P, et al. De novo nonsense mutations in ASXL1 cause Bohring-Opitz syndrome. Nat Genet 2011;43:729–31.
23. Bainbridge MN, Hu H, Muzny DM, Musante L, Lupski JR, Graham BH, et al. De novo truncating mutations in ASXL3 are associated with a novel clinical phenotype with similarities to Bohring-Opitz syndrome. Genome Med 2013;5:11.
24. Bak RO, Dever DP, Reinisch A, Hernandez DC, Majeti R, Porteus MH. Multiplexed genetic engineering of human hematopoietic stem and progenitor cells using CRISPR/Cas9 and AAV6. eLife 2017;6:18.
25. Inoue D, Matsumoto M, Nagase R, Saika M, Fujino T, Nakayama KI, et al. Truncation mutants of ASXL1 observed in myeloid malignancies are expressed at detectable protein levels. Exp Hematol 2016;44:172–6.
26. Wang L, Birch NW, Zhao Z, Nestler CM, Kazmer A, Shilati A, et al. Epigenetic targeted therapy of stabilized BAP1 in ASXL1 gain-of-function mutated leukemia. Nature Cancer 2021;2:515–26.

27. Newman AM, Steen CB, Liu CL, Gentles AJ, Chaudhuri AA, Scherer F, et al. Determining cell type abundance and expression from bulk tissues with digital cytometry. Nat Biotechnol 2019;37:773–82.
28. Litzenburger UM, Buenrostro JD, Wu B, Shen Y, Sheffield NC, Kathiria A, et al. Single-cell epigenomic variability reveals functional cancer heterogeneity. Genome Biol 2017;18:15.
29. Moudgil A, Wilkinson MN, Chen X, He J, Cammack AJ, Vasek MJ, et al. Self-reporting transposons enable simultaneous readout of gene expression and transcription factor binding in single cells. Cell 2020;182:992–1008.
30. Asada S, Goyama S, Inoue D, Shikata S, Takeda R, Fukushima T, et al. Mutant ASXL1 cooperates with BAP1 to promote myeloid leukaemogenesis. Nat Commun 2018;9:2733.
31. Skene PJ, Henikoff S. An efficient targeted nuclease strategy for high-resolution mapping of DNA binding sites. eLife 2017;6:e21856.
32. Fursova NA, Turberfield AH, Blackledge NP, Findlater EL, Lastuvkova A, Huseyin MK, et al. BAP1 constrains pervasive H2AK119ub1 to control the transcriptional potential of the genome. Genes Dev 2021;35:749–70.
33. Binder M, Carr RM, Lasho TL, Finke CM, Mangaonkar AA, Pin CL, et al. Oncogenic gene expression and epigenetic remodeling of cis-regulatory elements in ASXL1-mutant chronic myelomonocytic leukemia. Nat Commun 2022;13:1434.
34. Paczkowska M, Barenboim J, Sintupisut N, Fox NS, Zhu H, Abd-Rabbo D, et al. Integrative pathway enrichment analysis of multivariate omics data. Nat Commun 2020;11:735.
35. Zou Z, Ohta T, Miura F, Oki S. ChIP-Atlas 2021 update: a data-mining suite for exploring epigenomic landscapes by fully integrating ChIP-seq, ATAC-seq and Bisulfite-seq data. Nucleic Acids Res 2022;50:W175–82.
36. Schaefer EJ, Wang HC, Karp HQ, Meyer CA, Cejas P, Gearhart MD, et al. BCOR and BCORL1 mutations drive epigenetic reprogramming and oncogenic signaling by unlinking PRC1.1 from target genes. Blood Cancer Discov 2022;3:116–35.
37. Wang Z, Gearhart MD, Lee Y-W, Kumar I, Ramazanov B, Zhang Y, et al. A non-canonical BCOR-PRC1.1 complex represses differentiation programs in human ESCs. Cell Stem Cell 2018;22:235–51.
38. Walpole S, Pritchard AL, Cebulla CM, Pilarski R, Stautberg M, Davidorf FH, et al. Comprehensive study of the clinical phenotype of germline BAP1 variant-carrying families worldwide. J Natl Cancer Inst 2018;110:1328–41.
39. Ewens KG, Lalonde E, Richards-Yutz J, Shields CL, Ganguly A. Comparison of germline versus somatic BAP1 mutations for risk of metastasis in uveal melanoma. BMC Cancer 2018;18:1172.
40. Wunderlich M, Chou F-S, Sexton C, Presicce P, Chougnet CA, Aliberti J, et al. Improved multilineage human hematopoietic reconstitution and function in NSGS mice. PLoS One 2018;13:e0209034.
41. Conway E, Rossi F, Fernandez-Perez D, Ponzo E, Ferrari KJ, Zanotti M, et al. BAP1 enhances polycomb repression by counteracting widespread H2AK119ub1 deposition and chromatin condensation. Mol Cell 2021;81:3526–41.
42. Bartosovic M, Kabbe M, Castelo-Branco G. Single-cell CUT&Tag profiles histone modifications and transcription factors in complex tissues. Nat Biotechnol 2021;39:825–35.
43. Inoue D, Fujino T, Sheridan P, Zhang Y-Z, Nagase R, Horikawa S, et al. A novel ASXL1–OGT axis plays roles in H3K4 methylation and tumor suppression in myeloid malignancies. Leukemia 2018;32:1327–37.
44. Fujino T, Goyama S, Sugiura Y, Inoue D, Asada S, Yamasaki S, et al. Mutant ASXL1 induces age-related expansion of phenotypic hematopoietic stem cells through activation of Akt/mTOR pathway. Nat Commun 2021;12:1826.
45. Tyner JW, Tognon CE, Bottomly D, Wilmot B, Kurtz SE, Savage SL, et al. Functional genomic landscape of acute myeloid leukaemia. Nature 2018;562:526–31.
46. Shukla S, Ying W, Gray F, Yao Y, Simes ML, Zhao Q, et al. Small-molecule inhibitors targeting polycomb repressive complex 1 RING domain. Nat Chem Biol 2021;17:784–93.
47. Su W, Han HH, Wang Y, Zhang B, Zhou B, Cheng Y, et al. The polycomb repressor complex 1 drives double-negative prostate cancer metastasis by coordinating stemness and immune suppression. Cancer Cell 2019;36:139–55.
48. Li H, Durbin R. Fast and accurate short read alignment with Burrows–Wheeler transform. Bioinformatics 2009;25:1754–60.
49. Li H, Handsaker B, Wysoker A, Fennell T, Ruan J, Homer N, et al. The sequence alignment/map format and SAMtools. Bioinformatics 2009;25:2078–9.
50. Cibulskis K, Lawrence MS, Carter SL, Sivachenko A, Jaffe D, Sougnez C, et al. Sensitive detection of somatic point mutations in impure and heterogeneous cancer samples. Nat Biotechnol 2013;31:213–9.
51. Koboldt DC, Zhang Q, Larson DE, Shen D, McLellan MD, Lin L, et al. VarScan 2: somatic mutation and copy number alteration discovery in cancer by exome sequencing. Genome Res 2012;22:568–76.
52. Lai Z, Markovets A, Ahdesmaki M, Chapman B, Hofmann O, McEwen R, et al. VarDict: a novel and versatile variant caller for next-generation sequencing in cancer research. Nucleic Acids Res 2016;44:e108.
53. Cingolani P, Platts A, Wang LL, Coon M, Nguyen T, Wang L, et al. A program for annotating and predicting the effects of single nucleotide polymorphisms, SnpEff. Fly 2012;6:80–92.
54. Corces MR, Buenrostro JD, Wu B, Greenside PG, Chan SM, Koenig JL, et al. Lineage-specific and single-cell chromatin accessibility charts human hematopoiesis and leukemia evolution. Nat Genet 2016;48:1193–203.
55. McKeown MR, Corces MR, Eaton ML, Fiore C, Lee E, Lopez JT, et al. Superenhancer analysis defines novel epigenomic subtypes of non-APL AML, including an RARα dependency targetable by SY-1425, a potent and selective RARα agonist. Cancer Discov 2017;7:1136–53.
56. Mayakonda A, Lin D-C, Assenov Y, Plass C, Koeffler HP. Maftools: efficient and comprehensive analysis of somatic variants in cancer. Genome Res 2018;28:1747–56.
57. Miller CA, McMichael J, Dang HX, Maher CA, Ding L, Ley TJ, et al. Visualizing tumor evolution with the fishplot package for R. Bmc Genomics 2016;17:880.
58. Yu Y, Ouyang Y, Yao W. shinyCircos: an R/Shiny application for interactive creation of Circos plot. Bioinformatics 2017;34:1229–31.
59. Bak RO, Dever DP, Porteus MH. CRISPR/Cas9 genome editing in human hematopoietic stem cells. Nat Protoc 2018;13:358–76.
60. Clement K, Rees H, Canver MC, Gehrke JM, Farouni R, Hsu JY, et al. CRISPResso2 provides accurate and rapid genome editing sequence analysis. Nat Biotechnol 2019;37:224–6.
61. Schindelin J, Arganda-Carreras I, Frise E, Kaynig V, Longair M, Pietzsch T, et al. Fiji: an open-source platform for biological-image analysis. Nat Methods 2012;9:676–82.
62. Wickham H. Ggplot2. 2nd ed. Cham, Switzerland: Springer International Publishing; 2016.
63. Meers MP, Bryson TD, Henikoff JG, Henikoff S. Improved CUTRUN chromatin profiling tools. eLife 2019;8:e46314.
64. Langmead B, Salzberg SL. Fast gapped-read alignment with Bowtie 2. Nat Methods 2012;9:357–9.
65. Meers MP, Tenenbaum D, Henikoff S. Peak calling by sparse enrichment analysis for CUT&RUN chromatin profiling. Epigenetics Chromatin 2019;12:42.
66. Lun ATL, Smyth GK. csaw: a Bioconductor package for differential binding analysis of ChIP-seq data using sliding windows. Nucleic Acids Res 2016;44:e45.
67. Chen Y, Lun ATL, Smyth GK. From reads to genes to pathways: differential expression analysis of RNA-seq experiments using Rsubread and the edgeR quasi-likelihood pipeline. F1000Res 2016;5:1438.
68. Ramírez F, Ryan DP, Grüning B, Bhardwaj V, Kilpert F, Richter AS, et al. deepTools2: a next-generation web server for deep-sequencing data analysis. Nucleic Acids Res 2016;44:W160–5.
69. Zhu LJ. Integrative analysis of ChIP-Chip and ChIP-seq dataset. In: Lee T-L, Shui Luk AC, editors. Tiling arrays: methods and protocols. Totowa, NJ: Humana Press; 2013:105–24.
70. Li R, Huang D, Zhao Y, Yuan Y, Sun X, Dai Z, et al. PR-DUB safeguards Polycomb repression through H2AK119ub1 restriction. Cell Prolif 2023;e13457.

71. Melsted P, Booeshaghi AS, Liu L, Gao F, Lu L, Min KHJ, et al. Modular, efficient and constant-memory single-cell RNA-seq preprocessing. Nat Biotechnol 2021;39:813–8.
72. Bray NL, Pimentel H, Melsted P, Pachter L. Near-optimal probabilistic RNA-seq quantification. Nat Biotechnol 2016;34:525–7.
73. Soneson C, Love MI, Robinson MD. Differential analyses for RNA-seq: transcript-level estimates improve gene-level inferences. F1000Res 2015;4:1521.
74. Love MI, Huber W, Anders S. Moderated estimation of fold change and dispersion for RNA-seq data with DESeq2. Genome Biol 2014;15:550.
75. Gu Z, Eils R, Schlesner M. Complex heatmaps reveal patterns and correlations in multidimensional genomic data. Bioinformatics 2016;32:2847–9.
76. Corces MR, Trevino AE, Hamilton EG, Greenside PG, Sinnott-Armstrong NA, Vesuna S, et al. An improved ATAC-seq protocol reduces background and enables interrogation of frozen tissues. Nat Methods 2017;14:959–62.